# Giant electric-field-induced strains in lead-free ceramics for actuator applications – status and perspective

**Wook Jo · Robert Dittmer · Matias Acosta ·
Jiadong Zang · Claudia Groh · Eva Sapper · Ke Wang ·
Jürgen Rödel**

**Abstract** In response to the current environmental regulations against the use of lead in daily electronic devices, a number of investigations have been performed worldwide in search for alternative piezoelectric ceramics that can replace the market-dominating lead-based ones, representatively $Pb(Zr_xTi_{1-x})O_3$ (PZT)-based solid solutions. Selected systems of potential importance such as chemically modified and/or crystallographically textured $(K, Na)NbO_3$ and $(Bi_{1/2}Na_{1/2})TiO_3$-based solid solutions have been developed. Nevertheless, only few achievements have so far been introduced to the marketplace. A recent discovery has greatly extended our tool box for material design by furnishing $(Bi_{1/2}Na_{1/2})TiO_3$-based ceramics with a reversible phase transition between an ergodic relaxor state and a ferroelectric with the application of electric field. This paired the piezoelectric effect with a strain-generating phase transition and extended opportunities for actuator applications in a completely new manner. In this contribution, we will present the status and perspectives of this new class of actuator ceramics, aiming at covering a wide spectrum of topics, *i.e.*, from fundamentals to practice.

**Keywords** Giant electric-field-induced strain · Lead-free piezoceramics · Incipient piezoelectric · Relaxor ferroelectric · Actuator · Bismuth sodium titanate · Electric-field-induced phase transition

W. Jo (✉) · R. Dittmer · M. Acosta · J. Zang · C. Groh ·
E. Sapper · K. Wang · J. Rödel
Institute of Materials Science, Technische Universität Darmstadt,
Petersenstraße 23,
64287 Darmstadt, Germany
e-mail: jo@ceramics.tu-darmstadt.de

## 1 Introduction

Piezoelectricity is a physical phenomenon that allows inter-conversion between electrical and mechanical energy, leading to a number of applications wherever couplings between mechanical and electrical signals are required such as actuators, transducers, sensors, nano-positioners, ultrasonic motors and imaging devices, etc [1, 2]. As shown in Fig. 1(a), the year 2009 witnessed the global market for piezoelectric actuators of about 6,587 million US-$. The largest share was taken by applications related to ultra-small scale motion at about 48.6 %, followed by actuators for cameras and microscopes at 42.5 %. The remaining 8.9 % was distributed among fuel injectors (3.8 % share), micro-pumps (0.4 % share), ink cartridges (4.6 % share) and medical surgery instruments (0.2 % share). With an average annual growth rate of about 13 %, the market is expected to grow up to 12,290 million US-$ in 2014. The overall market shares remain relatively constant, but the overall share for fuel injectors is expected to grow from 3.8 % to 4.9 % in 2014. This increase reflects the requirements for achieving high fuel efficiency to meet the environmental regulations cast by the Euro emission standards [3]. For example, in the case of diesel engines, piezoelectric actuators exhibit more than five times faster response time than the conventional solenoid-based actuating modules and achieve more than 30 % fuel saving, about 25 % reduction of carbon dioxide emission, and 50 % increased torque [4].

From the materials' point of view, today's market for piezoactuators is largely dominated by PZT. About 98 % of the revenues generated in 2009 came from actuators made from bulk PZT and another 1 % from thick film PZT. The remaining 1 % is split among fiber composites, which are again mainly based on PZT, and lead-free materials. This dominant utilization of PZT is expected to remain till 2014.

Fig. 1 Global market shares of
piezoelectric actuators with
respect to (a) applications and
(b) materials [223]. The scale
bars on top of each plot denotes
the market size. Reproduction
of the data is under the kind
permission by Innovative
Research and Products, Inc
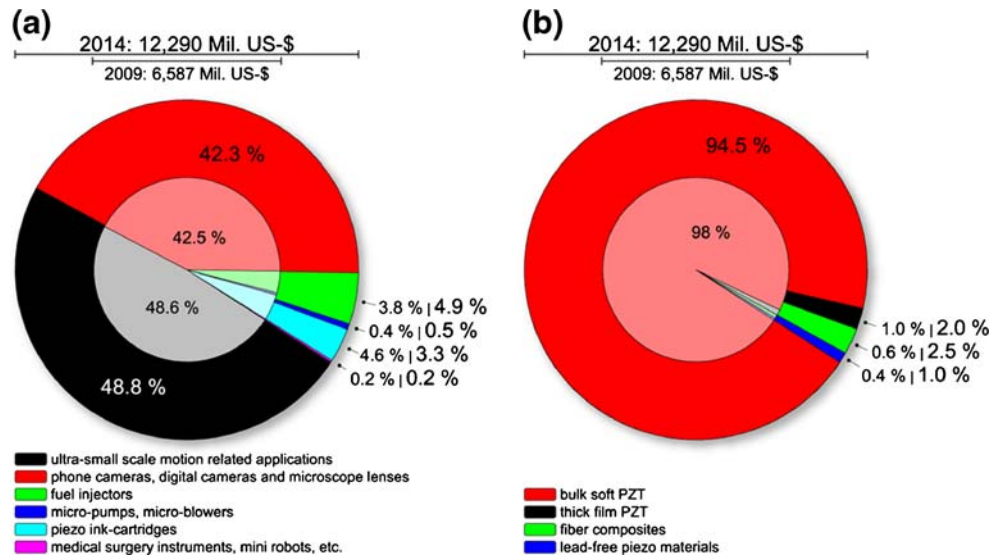


Thick film PZT (2.0 % share), fiber composites (2.5 %
share) and lead-free piezoelectric materials (1.0 %
share) are expected to grow at the expense of bulk PZT
which, however, will still represent 94.5 % of the market in
2014. Albeit on a low level, lead-free piezoelectric materials
will experience a strong average annual growth with more
than 30 %. At the moment, this statistics is heavily dependent
on quartz, $LiNbO_3$, and some prototype materials of potential
interest. However, the market situation is believed to change
in an unpredictable way in considering not only the impending
environmental regulations [5] but also the recent noteworthy
achievements in lead-free electro-strain ceramics, which will
be the main topic of the current paper.

The prospect of the lead-free electro-strain materials is
best-reflected in the number of publications as a function of
year up to 2011 (Fig. 2) [5–12]. The onset of the explosive
increase in the research activities can be traced back to the
discovery of the $(Bi_{1/2}Na_{1/2})TiO_3$-$BaTiO_3$ (BNT-BT) pseudo-
binary solid-solution system in 1991, where a morphotropic
phase boundary (MPB) resembling that of PZT was reported
by Takenaka's group [13]. Note that MPB is known to be one
of the key features in maximizing electromechanical proper-
ties of piezoelectrics [1, 14–18]. The explosion of the world-
wide research activities was triggered when Saito et al. [19]
reported that texturing via templated-grain-growth enabled
$(K_{0.5}Na_{0.5})NbO_3$ (KNN)-based piezoceramics to exhibit su-
perior electromechanical properties akin to PZT in 2004.
Special attention was given to the excellent temperature stabil-
ity of electromechanical properties of the textured KNN-based
ceramics. So far, a number of research works on the effect of
grain texturing both for KNN-based [20–22] and BNT-based
[23–32] systems have been reported, casting perspectives for
potential use for high-valued applications. In the meantime,
tuning the phase transition temperature from orthorhombic to
tetragonal by chemical modification has revealed that even the

properties of bulk KNN can be greatly enhanced, though KNN
still suffers a significant temperature-dependent variation in
functional properties [33–42].

Note that the trend in the number of publications study-
ing electric-field-induced strains of lead-free ceramics is
similar to that of the total publications in the field (inset in
Fig. 2). The statistics increases significantly especially on
bismuth-based systems as of 2007, when a giant electric-
field-induced strain was first reported in the $(Bi_{1/2}Na_{1/2})$
$TiO_3$-$BaTiO_3$-$(K_{0.5}Na_{0.5})NbO_3$ (BNT-BT-KNN) pseudoter-
nary solid-solution system [43–45]. Here, to avoid any
possible confusion, we confine the term, the giant electric-
field-induced strain, to the ones realized at the expense of
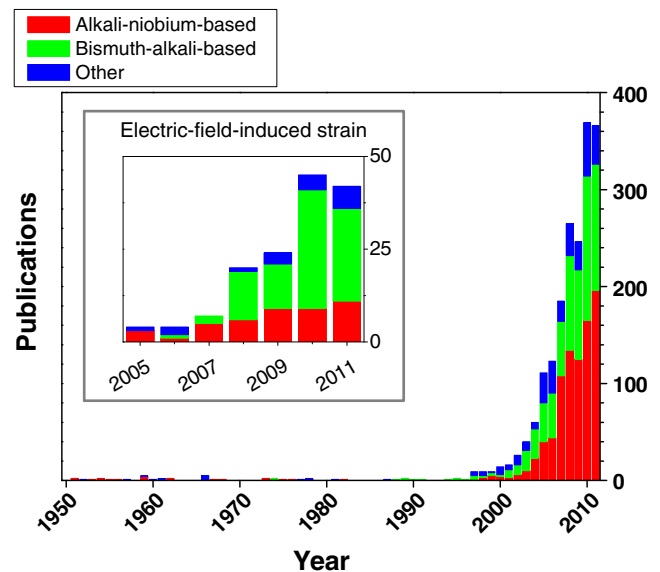


Fig. 2 The number of publications on lead-free piezoelectric materials
in total with that on studying electric-field-induced strains as a function
of year as an inset

poling-induced piezoelectricity. We refer to the material class that exhibits the giant electric-field-induced strain as incipient piezoceramics hereafter.[1] This finding highlighted the potential of this material for applications which require on/off-type high strokes, *e.g.,* fuel injectors.

When this giant electric-field-induced strain was first reported, it was subject to a couple of challenges for practical applications such as relatively large electric field required for activating it and considerably large strain hysteresis that may exclude some applications. In the meantime, to the scientific community, a big question mark was placed on the underlying mechanism. Initially, it was proposed based on the available literature that the strain comes from an antiferroelectric phase stabilized at room temperature due to chemical modifications [13, 51]. However, no experimental evidence supporting the assumption was found such as superlattice reflections due to multiplication of unit cell [52] or volume change as a consequence of antiferroelectric-to-ferroelectric phase transition on the application of electric field [53]. Instead, the average crystallographic symmetry was shown nothing but cubic [43, 54–56], and the volume change during the excursion of electrical cycling is reminiscent of usual ferroelectric materials [57]. Thus, it was proposed that the observed giant strain should have its origin in an electric-field-induced phase transformation from near 'non-polar' to a polar phase [57]. In situ neutron diffraction studies under electric field revealed that the material indeed underwent a phase transition from a near-cubic tetragonal phase, which is only distinguished by the presence of superlattice reflections from oxygen octahedral tilting [58], to a clearly non-cubic rhombohedral phase under electric field [59]. In situ transmission electron microscopy (TEM) experiments further corroborated that the initial pseudocubic phase lacks visible ferroelectric domains, while the application of electric field induces a clear contrast of lamella ferroelectric domains [60]. So far, it seems that all the experimental results converge to a conclusion that the giant strain comes from a reversible phase transition between relaxor and ferroelectric phase [18]. In this article, we attempt to sort out the existing controversies by reviewing the state-of-the-art, starting from the fundamentals of electric-field-induced strains to the up-to-date experimental achievements in lead-free electro-strain ceramics. This will be followed by a perspective for future research directions.

## 2 Electric-field-induced strains in perovskite materials

Ceramics with a perovskite structure have been of great interest to the community. Highly symmetrically-distributed constituting atoms allow the unit cell to deform easily giving rise to various ferroelectrically-active non-cubic phases such as tetragonal, rhombohedral, orthorhombic or monoclinic. The presence of interstitial sites and relatively large spatial tolerance for substitutional atoms are beneficial for chemical modifications, enabling one to tailor functional properties. When an external electric field is applied, these perovskite-structured ceramics are deformed with the changes in their macroscopic polarization state. Three representative electric-field-induced deformation behaviors that are expected in perovskite materials are shown in Fig. 3.

Figure 3(a) top and bottom show the polarization and strain hysteresis loops of a BNT-based material, featuring an electrostrictive behavior. In principle, all the dielectric materials show electrostrictive behavior including materials with center of symmetry. Since the electrostriction is negligibly small in the presence of piezoelectricity, this effect is best-seen in paraelectric materials. In this discussion, we use the term electrostrictive to specifically refer to the materials in the paraelectric state. A paraelectric material at a temperature that is sufficiently higher than its Curie point is polarized when an external electric field is applied. The induced polarization ($P$) is proportional to the product of the dielectric susceptibility ($\chi$) and the applied electric field ($E$), and thus expressed as

$$P = \varepsilon_0 \cdot \chi \cdot E, \qquad\qquad (1)^2$$

where $\varepsilon_0$ denotes the dielectric permittivity of vacuum. Since $\chi$ is constant in linear dielectrics such as paraelectric materials, $P$ is directly proportional to $E$, and thus $P$ has a linear dependence on $E$ as seen in Fig. 3(a) top. Strain originating from electromechanical coupling is, in general, expressed as a power series of electric field, which reads [61–63]

$$S = \alpha E + \beta E^2 + \gamma E^3 + \delta E^4 + \cdots. \qquad\qquad (2)$$

Because the electrostrictive deformation in paraelectric materials vanishes on the removal of electric field, the electrostrictive strain is always positive regardless of the field direction, as long as the material belongs to linear dielectrics [64]. This is a distinct feature, rendering it different

---

[1] In the ferroelectric society, the term, incipient ferroelectrics, has been used to refer specifically to 'quantum paraelectrics,' [46] though the word 'incipient' has been used in many disciplines in a broader sense, *e.g.*, the incipient stage of a fever in medicine [47], incipient cracks or incipient dislocations in mechanics [48], incipient phase separation in thermodynamics [49], *etc*. Here, the term 'incipient' is used, conforming to the definition as given in Oxford and Webster: 'beginning to happen or develop.' Likewise, the currently introduced class of materials can be termed as 'incipient piezoceramics' in that initially small piezoelectricity begins to develop with the application of electric field [50]. The relevance of designating incipient piezoceramics to the ceramics of current interest becomes apparent in the succeeding sections.

[2] Rigorously speaking, tensor notation is required in expressing the entities such as polarization, susceptibility, electric field, strain, etc., but is removed for simplicity here.

**Fig. 3** Three archetypal polarization (top row) and strain (bottom row) hysteresis loops in perovskite-structured materials. (**a**), (**b**), and (**c**) are measured with the measurement frequency of 50 mHz during poling at room temperature on electrostrictive 0.54BNT-0.36BT-0.10KNN, a commercial ferroelectric PZT (PIC151, PI Ceramics), and antiferroelectric $Pb_{0.99}Nb_{0.02}[(Zr_{0.57}Sn_{0.43})_{0.7}Ti_{0.3}]_{0.98}O_3$ (PNSZT), respectively
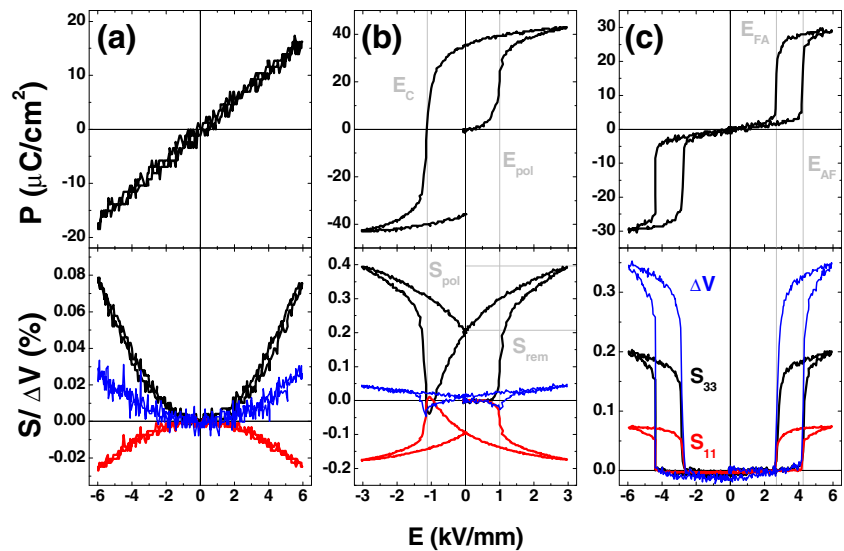


from the piezoelectric strain. This leaves out all the terms of the odd degrees in the electrostrictive effect in Eq. 2. With shear components ignored, Eq. 2 is reduced simply to a quadratic function of electric field.

$$S = \beta E^2 + \delta E^4 + \cdots \simeq \beta E^2, \tag{3}$$

From Eq. 1, Eq. 3 is alternatively written as [63, 65]

$$S = QP^2, \tag{4}$$

where $Q$ is the commonly quoted electrostrictive coefficient. During electrical cycling, the material undergoes a Poisson's ratio-type deformation with $-S_{11}/S_{33}$ being constant (~0.3 for the currently presented material), leading to a quadratic increase in volume [1].

Figure 3(b) top and bottom show polarization and strain hysteresis loops in ferroelectric ceramics, respectively, which are normally observed during the poling process. In the unpoled state, the material is not macroscopically piezoelectric, yet. When an electric field is applied, however, the material follows an electrostrictive behavior when the applied field is small. Around the so-called poling field ($E_{pol}$) that can be defined at the inflection point in the polarization hysteresis loop and is often slightly different from the coercive field ($E_c$) [57, 66], a massive alignment of randomly-oriented ferroelectric domains occurs along the field direction by switching its polarity towards one of the energetically equivalent directions nearest to the field direction with the spontaneous polarization value being asymptotically approached. With the removal of the applied electric field, a fraction of reoriented ferroelectric domains gradually switch back depending on their energetic stability, leaving the material to reach a remanent state at zero electric field. With this remanent state after poling, materials can be used for piezoelectric applications. In an ideal defect-free single crystal that is poled perfectly, the remanent strain is

represented by its lattice distortion. For example, soft PZT $Pb_{0.99}(Zr_{0.45}Ti_{0.47}(Sb_{0.67}Ni_{0.33})_{0.08})O_3$ (PIC151, Lederhose, Germany), which consists mainly of tetragonal phase, is estimated to show 1.5 % ($c/a$ ratio=1.0154) as $S_{rem}$, though the experimentally observed $S_{rem}$ as shown in Fig. 3(b) is about 0.2 % (13 % of the ideal value) [67]. This deviation can be attributed to many different origins such as randomness of grain orientations which naturally confine the orientation of domains, depolarization fields arising from defects, pinning of domains, *etc*.

It is interesting to note that ferroelectricity enables polycrystalline materials to exhibit piezoelectricity, but this very ferroelectricity limits the level of practically achievable displacement bound by the difference between $S_{pol}$ and $S_{rem}$. One should notice that different from the remanent polarization that is easily estimated by the usual polarization hysteresis loop measurements, the magnitude of $S_{rem}$ just like $E_{pol}$ is only determinable during this very first cycle, *i.e.*, the poling cycle, since the reference state, *i.e.*, the virgin state, is only known from the poling cycle. Ironic as it may be, the larger the $S_{rem}$ ($P_{rem}$), the larger the piezoelectric coefficient ($d_{33}$) but the smaller the achievable maximum strain level becomes; thus, the standard practice of quantifying actuating performance with the piezoelectric coefficient may be inappropriate. The strain of practical importance for most actuator applications is given merely by the difference between $S_{pol}$ and $S_{rem}$. On the other hand, when the field direction is reversed, materials contract until collective domain switching occurs at $E_c$. Here, the difference between the $S_{rem}$ and the minimum strain level, *i.e.*, $S$ at $E_c$, is termed negative strain ($S_{neg}$) in that this strain is only visible when a 'negative' field is applied, *i.e.*, in bipolar driving mode [44, 57]. The magnitude of $S_{neg}$ depends largely on the competition between 180° and non-180° domain switching processes. The more the non-180° domain switching takes place, the deeper the $S_{neg}$ extends. It is seen

that the simultaneously measured radial strain mirrors the axial strain at a smaller magnification, resulting in a volume hysteresis representing hydrostatic piezoelectric contribution [68].

Some compositions represented by $PbZrO_3$ [69, 70], $NaNbO_3$ [71–73], and $AgNbO_3$ [74, 75] are known to be energetically stable when spontaneously polarized rows of ions are aligned alternatingly such that the macroscopic net polarization becomes zero [76]. These materials lack piezoelectricity due to the presence of center of symmetry, which distinguishes this class of materials from ferroelectrics under the name antiferroelectrics. When the free energy between ferroelectric and antiferroelectric state is comparable, an externally applied electric field can induce a ferroelectric state out of an antiferroelectric state, which results in a double hysteresis in the polarization hysteresis loop. This is exemplarily shown for an antiferroelectric $Pb_{0.99}Nb_{0.02}[(Zr_{0.57}Sn_{0.43})_{0.7}Ti_{0.3}]_{0.98}O_3$ (PNZST) in Fig. 3(c) top [77]. In analogy with the poling process of ferroelectrics, the inflection point encountered during increasing and decreasing electric field can be termed as antiferroelectric-to-ferroelectric switching field ($E_{AF}$) and ferroelectric-to-antiferroelectric switching field ($E_{FA}$), respectively. Hence, engineering $E_{AF}$ and $E_{FA}$ is critical for practical applications such as digital displacement transducer, energy storage capacitor, solid-state cooling devices, etc [78]. Note that the reversible transition between the antiferroelectric and ferroelectric state involves appearance and disappearance of center of symmetry with a different packing density of unit cell, resulting in a volume change as shown in Fig. 3(c) bottom [53]. This volume change is known to be the main cause of the electric-field-induced strain in antiferroelectric materials [79]. It is known that the electric-field-induced ferroelectric phase either converts back to antiferroelectric phase completely or stays partially as a metastable phase depending on the mechanical boundary condition that could impede the transition [77, 78, 80]. The presence of piezoelectricity out of near- or non-polar phase with electric field classifies the antiferroelectric ceramics as incipient piezoceramics.

In practice, the electric-field-induced strains are often affected by various factors depending on the phase transition temperature [81–84] or types of defects [85, 86], both of which cause corresponding macroscopic signals to deviate from the aforementioned well-established shapes. One of the most commonly observed is a constriction or doublet of the polarization hysteresis loops, which often leads to a significant enhancement in the maximum usable strains during unipolar cycling. The following introduces a representative example for each case.

Figure 4 presents the polarization hysteresis loops of a BT single crystal measured near the Curie point [81]. The polarization hysteresis loop at room temperature displays a typical square shape with a well-defined coercive field at ~0.16 kV/mm. However, once the temperature is increased
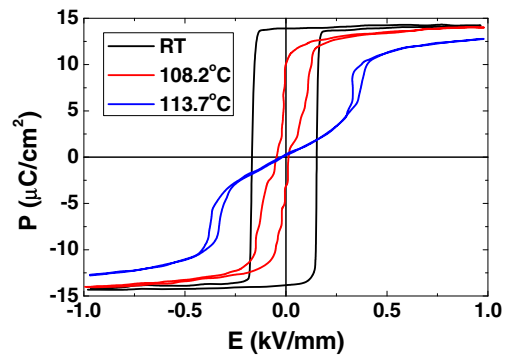


**Fig. 4** Changes in the polarization hysteresis of BT single crystal [81]. The Curie temperature of the given crystal determined by a dielectric permittivity measurement is 107.5 °C

beyond the Curie point, the polarization hysteresis loop starts to deviate from its usual square shape with a constriction developing, leading eventually to a double hysteresis with further increase in the temperature. The result implies that thermally-induced disruption of ferroelectricity can be restored by the application of external electric field, and the observed double hysteresis loop is the consequence of this field-induced phase transition from paraelectric to ferroelectric phase.

In fact, this type of behavior was already predicted by the Ginzburg-Landau-Devonshire model. Following Merz [81], the free energy ($A$) of stress-free ferroelectrics as a function of polarization ($P$) is expressed:

$$A = \alpha(T - T_0)P^2 + \beta P^4 + \gamma P^6, \tag{5}$$

where $\alpha$, $\beta$, $\gamma$, and $T_0$ are material-dependent constants and extrapolated temperature (Curie-Weiss temperature) from the reciprocal susceptibility plot, respectively. The derivative of $A$ with respect to $P$ yields a relationship between electric field ($E$) and $P$.

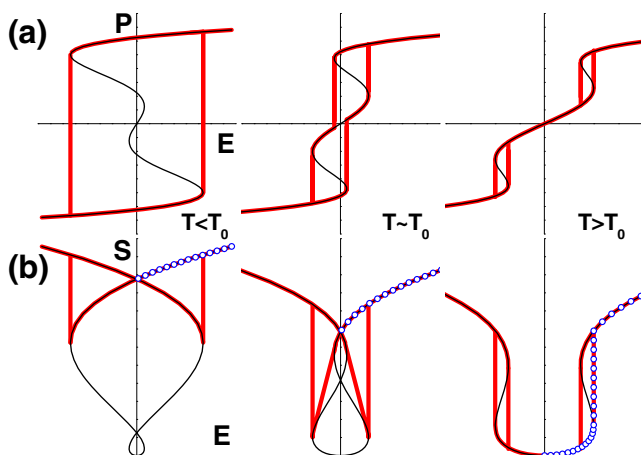$$\partial A/\partial P = E = 2\alpha(T - T_0)P + 4\beta P^3 + 6\gamma P^5 \tag{6}$$

By normalizing $E$ and $P$ into dimensionless $e$ and $p$, Eq. 6 reduces to a polynomial function with the dimensionless temperature $t$ as single variable:

$$e = 2tp - 4p^3 + 2p^5, \tag{7}$$

where $e = (27\gamma^3/\beta^5)^{1/2}E$, $p = (3\gamma/\beta)^{1/2}P$, and $t = (3\alpha\gamma/\beta^2)(T - T_0)$. By adjusting $t$ appropriately, all the experimentally observed polarization hysteresis loops in Fig. 4 can be simulated as presented in Fig. 5(a). Below $T_0$, the polarization hysteresis assumes a square shape that is common for normal ferroelectrics. However, the polarization hysteresis starts to be pinched above $T_0$, i.e., an incipient piezoelectric state, eventually evolving into a double hysteresis with further increasing temperature. The deformation of the polarization hysteresis loop is the consequence of electric-field-induced stabilization of a metastable ferroelectric phase

out of a paraelectric phase. It is unfortunate that experimental works to the effect of this field-induced phase transition on strain hysteresis are not available in the literature. Nevertheless, a rough estimation of strain hysteresis is possible using the Ginzburg-Landau-Devonshire model. When the stress free situation of a single crystal with a single domain is concerned, the bulk experiences only the polarization-induced spontaneous strain, which has been shown for most ferroelectric ceramics to have a quadratic dependence on the polarization to a dominating order [2, 61, 62]. For a qualitative investigation of the strain hysteresis, therefore, one can examine the response of the square of the polarization with respect to the electric field. The bipolar strain hysteresis loop corresponding to each polarization hysteresis loop given in Fig. 5(a) can be estimated as depicted in Fig. 5(b) with unipolar strains being denoted by a circular symbol. The appearance of constriction in the polarization hysteresis prompts significant enhancement in unipolar strain with a rapid decrease in $S_{rem}$. When the polarization hysteresis loop splits into a double loop, the corresponding strain hysteresis changes from a typical butterfly shape of ferroelectrics to a so-to-speak 'sprout' shape without $S_{neg}$. Due to a drastic increase in the electric field required to nucleate the metastable ferroelectric phase out of the paraelectric state with temperature, however, this phenomenon is normally observed in a narrow temperature window, severely limiting the use of the phenomenon for practical applications.
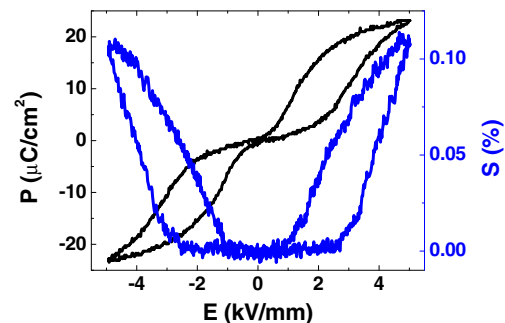
It is well-known that aliovalent doping has great impact on the functional properties of ferroelectric materials [10]. Especially in the case of acceptor doping in PZT-based materials, a significant change in macroscopic properties results [87–91]. For example, when $Fe^{3+}$ replaces either $Zr^{4+}$ or $Ti^{4+}$ in PZT, the polarization hysteresis is significantly affected with the introduction of an internal bias field that tends to counteract the effects of external fields [85, 92–94]. The origin of the internal bias field is still controversial between free charge carriers accumulating at domain walls [95, 96], highly associated defect dipoles aligning preferentially [86, 97], or collective contribution of both [98], but it is generally accepted that this internal bias field causes the polarization hysteresis loop to become constricted. Figure 6 exemplifies the influence of highly associated defect dipoles on macroscopic properties [87]. Due to the presence of acceptor-induced defects, the material has a resistance to the poling process, resulting in a pinched polarization hysteresis loop with a negligible remanent strain; thus, again, a sprout-shaped strain hysteresis results. Therefore, this defect-induced change can also lead to an apparent enhancement in the unipolar strain as exemplarily demonstrated in several systems [45, 48, 50]. However, it is highly uncertain that this phenomenon can be used in real applications due to its vulnerability against repetitive cycling.

In spite of the apparent similarity in the macroscopic properties with antiferroelectric materials and paraelectric materials near the Curie point, this class of materials is distinct by a couple of unique features. The defect-induced polarization double hysteresis loop can be deformed into a highly anisotropic shape by removing the 'randomness' of locally existing internal bias fields through thermally-activated poling process as exemplarily shown in Fig. 7(a) [10]. The constriction in the polarization hysteresis loops is further affected by repeated electrical cycling as presented in Fig. 7(b) [85, 87]. With increasing cycle number, the constricted hysteresis loop is seen to transform into a commonly expected square shape. This change also has an impact on the corresponding strain hysteresis loop given in Fig. 7(c) [87]. With continuous cycling, the onset field of noticeable strain gradually decreases, and eventually a typical butterfly-shaped strain curve is restored. As noted, the gradual increase in the maximum polarization value and total strain level (even the unipolar strain) with cycle number clearly indicates that the defect-induced changes in the polarization and strain are due to highly suppressed domain switching; thus, the seemingly large unipolar strain in the presence of constriction is, in fact, only a part of the maximum attainable strains in the



Fig. 5 (a) Polarization and (b) strain hysteresis loops near the Curie temperature predicted by Ginzburg-Landau-Devonshire model. Thin and thick lines represent the traces of Eq. 7 and the actual signals that are expected to be observed in practice



Fig. 6 Polarization and strain hysteresis loops of Fe-doped PZT after a reduction treatment for 2 h [87].

**Fig. 7** (**a**) Polarization hysteresis of so-called hard PZT after high temperature poling process that forcefully aligns defect dipoles along a preferential direction [10] as well as changes in a (**b**) polarization and (**c**) strain hysteresis loop as a function of electrical cycling [87]. The number of cycle is 1, 1000, and 10000 along the direction of arrows
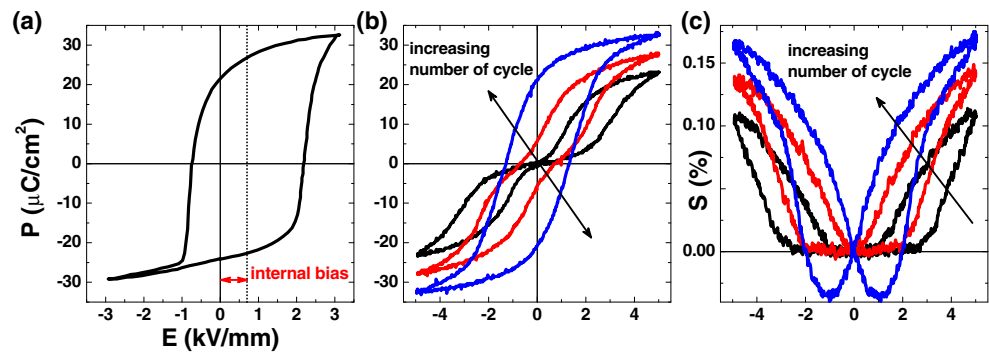
given materials. It is expected that practical use of the phenomenon is severely limited in that the material properties are highly susceptible to the conditions for sample preparation such as cooling rate, storage time between preparation and characterization, *etc.* as well as operational conditions such as cycling profiles.

## 3 Electric-field-induced strain in lead-free ceramics

This section first compares three representative lead-free systems to emphasize why BNT-based materials received a special spotlight as a potential for high stroke actuator applications. Then, an overview over the features of BNT-based incipient piezoceramics will be followed. Experimental results are then utilized to rationalize the properties observed.

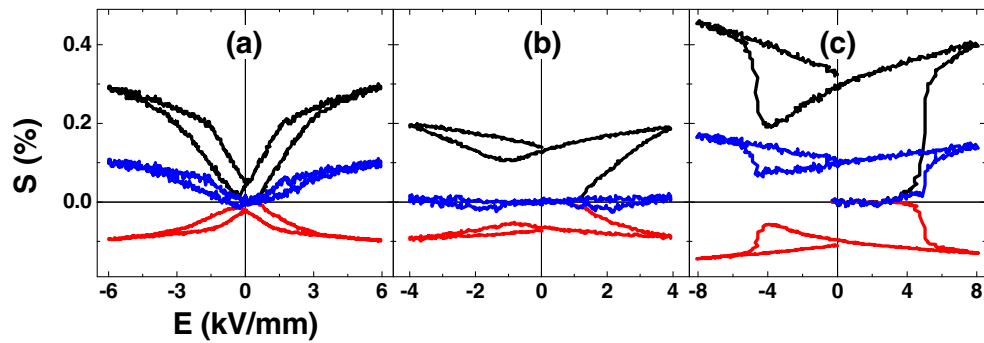### 3.1 Electric-field-induced strains in lead-free piezoceramics

So far, extensive research activities over decades have been devoted to searching for new compositions in lead-free piezoceramics that could compete against the PZT-based piezoceramics. In spite of the majority of choices in the periodic tables, not many systems other than three base-systems, *i.e.*, $BaTiO_3$ (BT), $(K_{0.5}Na_{0.5})NbO_3$ (KNN), and $(Bi_{1/2}Na_{1/2})TiO_3$ (BNT) have been deemed competitive [5]. As discussed in the previous section, $S_{max}/E_{max}$ as a figure of merit for high stroke actuators is estimated by $(S_{pol}-S_{rem})/E_{max}$. The higher the $S_{pol}$ and the lower the $S_{rem}$ are, the better the actuating performance is. Of course, the lower the $E_{max}$ is, the higher the performance is also. Therefore, the potentiality of material systems for actuator applications can be best-seen by the saturated strain hysteresis loop measured during the poling cycle.

Figure 8(a)–(c) presents the strain hysteresis curves of three representative lead-free ceramics, *i.e.*, pure BT, pure KNN, and pure BNT during a bipolar poling cycle at room temperature. To have a sound comparison, the strain curves were measured at an electric field as high as possible so that comparison for the potentiality of each material is feasible. Due to a small poling field at ~0.45 kV/mm and coercive field at ~0.3 kV/mm, BT shows fairly large strain with a very small

hysteresis. It is noted that with its small $S_{rem}$ at ~0.02 %, the strain of BT leads to a normalized strain, $S_{max}/E_{max}$, of as large as 594 pm/V at the field strength of 2.6 kV/mm at room temperature, indicating why extraordinarily enhanced piezoelectric performance can be achieved in its derivative compositions [99]. The concurrently measured radial strain has a mirror image to the axial strain with a smaller magnitude, resulting in a volume change during electrical cycling. A relatively large volume change reaching up to ~0.1 % at 6 kV/mm implies a high potentiality for hydrophone applications, whose figure of merit is given by the hydrostatic piezoelectric coefficient, $d_h$. $d_h$ is defined as $d_{33}+2·d_{31}$, which is related to the volume change under electric field [100–103]. Apart from the fact that BT suffers from its relatively low Curie point (~110 °C for the currently prepared BT ceramics [104]) that limits practical applications, BT is one of the best piezoceramics so far.

Pure KNN presented in Fig. 8(b) has a relatively small poling strain of ~0.19 % at 4 kV/mm with $E_{pol}$ and $E_c$ being at ~1.5 kV/mm and at ~1 kV/mm, respectively. The poling behavior of KNN is similar to that of BT in the sense that no significant change before and after $E_{pol}$ is denoted, but it is clearly different in that $S_{rem}$ is high with ~0.13 % indicating that the switching kinetics of domains is very sluggish at room temperature. $S_{max}/E_{max}$ in unipolar driving mode is 150 pm/V with a potentially achievable $S_{max}/E_{max}$ of 475 pm/V if $S_{rem}$ can be tuned to zero. In addition, the volume change during cycling is extremely small, rendering the material not attractive for hydrophone applications.

Pure BNT gives enormously large $S_{pol}$ at ~0.4 % at 8 kV/mm, which is almost two times larger than in the other two systems. However, it suffers from a large poling field of ~5.5 kV/mm; thus, the poling treatment at 8 kV/mm at room temperature is insufficient to induce a stable poling state, which is indicated from the increasing $S_{max}$ value during cycling, *e.g.*, $S_{max}$ at −8 kV/mm>$S_{max}$ at 8 kV/mm. In addition, $S_{rem}$ is high at ~0.23 % rendering $S_{max}/E_{max}$ at only ~213 pm/V. However, the obtainable $S_{max}/E_{max}$ is as large as 500 pm/V. A feature making BNT unique among the others is the presence of remanent volume after electrical poling, which strongly suggests that pure BNT undergoes an irreversible

**Fig. 8** Electric-field-induced strains of (**a**) pure BT, (**b**) pure KNN, and (**c**) pure BNT with the associated volume change, measured during bipolar poling cycle at 50 mHz. Note that the maximum electric field applied for BNT is larger at 8 kV/mm than that 6 kV/mm for BT and at 4 kV/mm for KNN. BT was sintered at 1350 °C for 2 h using a commercial powder (99.5 %, Ferro Crop., N.Y., U.S.A.). KNN and BNT were sintered at 1080 °C for 3 h and 1150 °C for 3 h, respectively, using calcined powders prepared by solid-state reaction method using elemental carbonates and oxides (>99 %, Alfa Aesar, Karlsruhe, Germany)

electric-field-induced phase transition that should involve a crystallographic symmetry change [68].
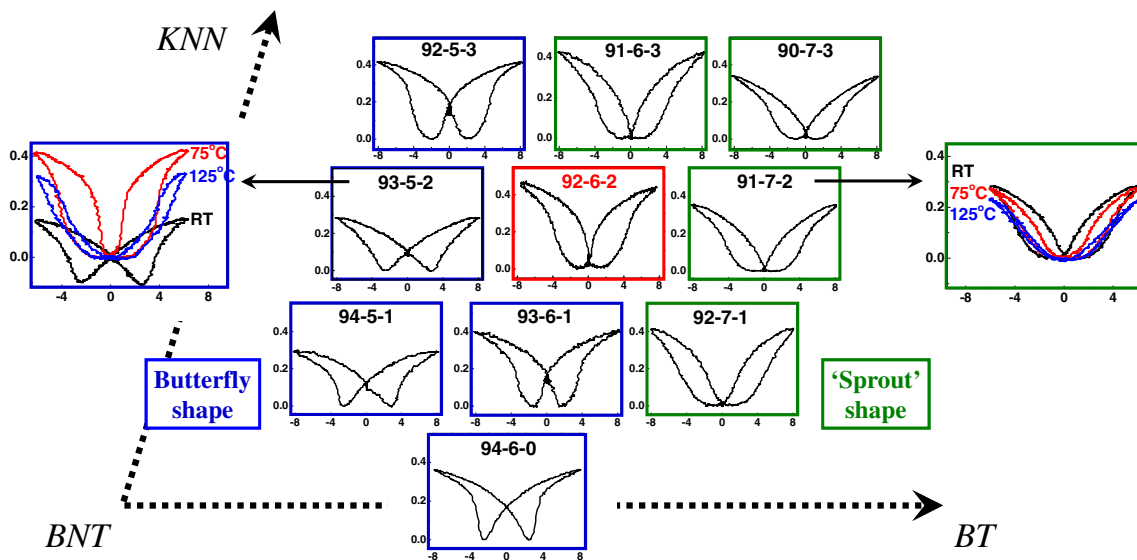
### 3.2 Giant electric-field-induced strain in BNT-BT-KNN

The birth of scientific interest from the community in giant electric-field-induced strain dates back to 2007 when Zhang et al. [43] reported 0.45 % of unipolar strain at 8 kV/mm in the KNN-modified BNT-BT system. The reported giant strain can be characterized with the following seven features.

1) This giant strain is activated above a certain threshold electric field [43, 44].
2) It involves a considerably large hysteresis [43, 44].
3) X-ray structure of the material is nothing but cubic [43].

4) No ferroelectric domain is visible in as prepared samples [44].
5) It is only available when macroscopic piezoelectricity nearly vanishes [43, 44]. At this point, the typical butterfly-shaped strain hysteresis transforms into a sprout-shaped one [44].
6) Its emergence is closely related to a high temperature polymorph [45].
7) This large strain decays rather slowly over a wide range of temperature [45].

The characteristics of the giant strain in BNT-BT-KNN system can be best-visualized with the composition-dependent strain hysteresis loops as in Fig. 9. The initial plan for the use of the pseudoternary system was to couple



**Fig. 9** Bipolar strain hysteresis of BNT-BT-KNN pseudoternary system near the known 'MPB' composition, 0.94BNT-0.06BT. The maximum electric-field-induced strain appears at a boundary where butterfly-shaped hysteresis loops indicative of dominant ferroelectric order change into 'sprout'-shaped ones implying the presence of macroscopically 'non-polar' phase at zero electric field. The temperature-dependent hysteresis loops of selected compositions as appended suggest that the alleged 'non-polar' phase be a high-temperature polymorph of the given system

two MPB compositions such as 0.94BNT-0.06BT [13] and 0.94KNN-0.06BT [105, 106] to maximize the electromechanical properties of the given system [5]. Unexpected, however, the addition of the third component 0.94KNN-0.06BT into 0.94BNT-0.06BT resulted in a rapid decrease in piezoelectricity represented by $d_{33}$ and the appearance of a giant strain [43, 44]. This strain behavior was maximized in compositions at a boundary between butterfly-shaped strain hysteresis loops and sprout-shaped ones. Temperature-dependent strain measurements demonstrated that the birth of giant strain was closely related to the high-temperature polymorph of the system [45].

Later, the source for the giant strain was revealed by temperature-dependent bipolar poling strain measurements [57]. As implied by the previous temperature dependent strain measurements that the appearance of giant strain in 0.92BNT-0.06BT-0.02KNN is due to the stabilization of the high temperature polymorph [45], a nearby composition, 0.93BNT-0.06BT-0.01KNN, was selected for the experiment. As seen in Fig. 10, two parameters, i.e., $S_{pol}$ and $S_{rem}$, decrease with increasing temperature. However, the rate of change in $S_{rem}$ exceeds $S_{pol}$, leading to a peak value in the difference between them which defines the figure of merit for actuating performance, $S_{max}/E_{max}$, during unipolar cycling. It implies that the giant strain originates from a destabilization of ferroelectricity in the absence of electric field. This categorizes the BNT-BT-KNN materials as incipient piezoceramics in that the material has initially weak piezoelectricity which is strengthened as a function of electric field. The transformation of weak piezoelectricity into strong piezoelectricity can be demonstrated by measuring the small signal piezoelectric coefficient as a function of electric field, as exemplarily shown in $Bi(Zn_{1/2}Ti_{1/2})O_3$-modified BNT-BKT [50]. As a reminder, both the aforementioned field-induced phase transition of the antiferroelectric PNZST and the paraelectric BT transforming into ferroelectric slightly above the Curie point also characterize an incipient piezoceramic. It is noted that in comparison to the paraelectric BT, 0.92BNT-0.06BT-0.02KNN exhibits relatively good temperature stability in its unipolar strain,

e.g., it varies from 0.32 % at 27 °C to 0.13 % at 200 °C [45]. This suggests that the phase responsible for the giant strain in BNT-based materials is different from a pure paraelectric state.

The nature of the assumed 'non-polar' phase was further analyzed by transmission electron microscopic study using a specially devised sample holder that allows in situ environment for the application of large electric fields [60]. The major discovery of the study is summarized in Fig. 11. When the material was not exposed to any external electric field (Fig. 11(a)), two coexisting superlattice reflections indicative of oxygen octahedral tilting allowed in rhombohedral and tetragonal symmetry were observed within a single grain. The grain contrast was homogeneous with a 'grainy' structure implying the presence of nanoscale features. However, neither ferroelectric nor antiferroelectric domain configuration was evidenced, which is consistent with other transmission electron microscopic investigations on similar compositions [107]. When an appropriate level of electric field (actual field level of 5 kV/mm) was applied, a clear lamella contrast indicating ferroelectric domains develops with a bending contrast due to the converse piezoelectric effect as depicted in Fig. 11(b). With the appearance of clear domain contrast, the superlattice reflections indicative of rhombohedral $R3c$ symmetry became intensified. On the removal of electric field, the induced lamella domain contrast disappeared, leaving strain-induced bending contrast and dislocations (Fig. 11(c)).

Follow-up experiments using in situ X-ray and neutron diffraction techniques confirmed that there is an electric-field-induced reversible phase transition, as depicted in Fig. 12 [59]. The initially highly symmetric (110)pc (pc denotes pseudocubic) reflection starts to split up at about 2.2 kV/mm. Upon removal of the electric field, the induced splitting disappears and the initial configuration is restored, which confirms that the observed electric-field-induced phase transition is reversible. In agreement with the in situ transmission electron microscopic experiment [60], the field-induced phase was identified as a rhombohedral phase with $R3c$ space group. A high resolution X-ray and neutron diffraction conducted prior to the in situ experiments



**Fig. 10** (a) Temperature-dependent bipolar poling curves of 0.93BNT-0.06BT-0.01KNN and (b) a summary of selected parameters [57]. A sharp increase in $S_{max}/E_{max}$ results from a rapid decrease in $S_{rem}$ with increasing temperature
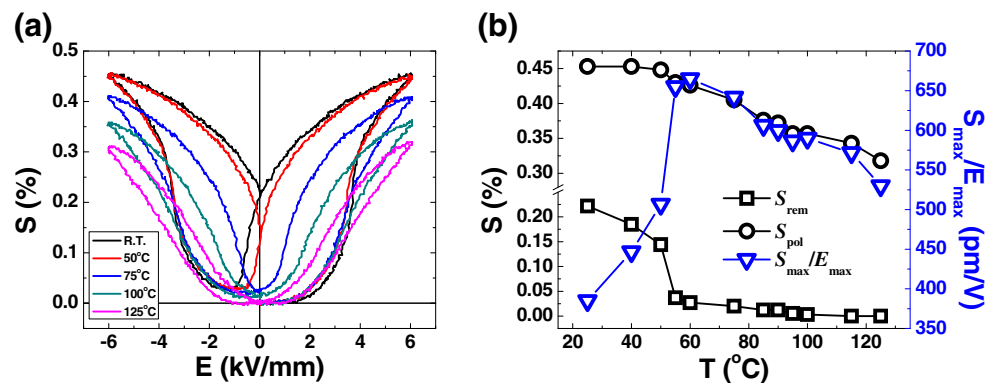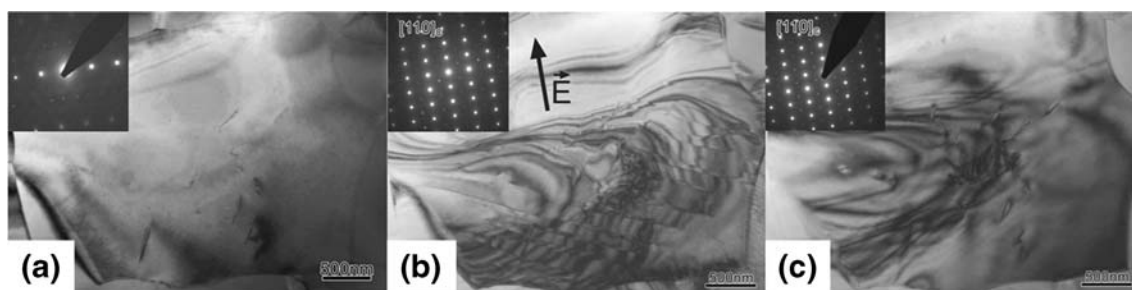
**Fig. 11** In situ transmission electron microscopy of 0.91BNT-0.06BT-0.03KNN under electric field. (**a**) Initial state at 0 kV/mm, (**b**) at ~5 kV/mm, and (**c**) final state at 0 kV/mm

suggested that the phase identity of 0.92BNT-0.06BT-0.02KNN at zero electric field could be tetragonal, although no obvious peak splitting indicative of the presence of non-cubic distortion was evident. The tetragonality was so small ($c/a = 1.0003$) that the designation of tetragonal symmetry was only based on superlattice reflections [59], which are commonly interpreted as in-phase oxygen octahedral tilts [58]. Different from the in situ transmission electron microscopic investigations [60, 107], little trace of superlattice reflections indicating rhombohedral symmetry was detected in virgin state possibly due to insufficient counting statistics. Again here, no supporting evidence for antiferroelectricity was found. In fact, centrosymmetric space groups such as *P4/mbm* failed in fitting the obtained superlattice reflections, which actually disfavors the antiferroelectric assumption. Note that even though the symmetry at zero electric field was designated as tetragonal with reference to superlattice reflections, the observed superlattice reflections do not necessarily represent the average long-range symmetry of the system. In fact, the observed superlattice reflections were considerably broader than Bragg reflections, which indicates a decoupling between two reflection types. Particle size based on superlattice reflections was estimated to be

~8 nm, which is by far smaller than the average grain size of ~2 μm. It follows that the detected tetragonal symmetry may represent the symmetry existing and persisting only at a very local scale; thus, the average long-range symmetry may be, indeed, cubic. These results together with those from the in situ transmission electron microscopic studies strongly suggest that the BNT-BT-KNN system with giant strains should be understood as a relaxor ferroelectric. It is well-known that relaxor materials commonly exhibit a cubic symmetry in average with the presence of non-cubicity below the detection limit of X-ray diffraction techniques [108–110].

In the meantime, questions on the phase identity were also raised on the base BNT-BT system, because, contrary to common expectation, BNT-BT also displays a cubic symmetry especially near the MPB regions [43, 56]. In fact, the phase stability and identity of the BNT-BT system is so complicated that in addition to the initially proposed phase diagram by Takenaka et al. [13], at least five more phase diagrams have been proposed [111–115]. A clue to resolve the complexity of the BNT-BT system was given by Daniels et al. [55], who demonstrated utilizing in situ electric-field-dependent diffraction technique on compositionally-graded specimen that the average structure of nominally 0.93BNT-
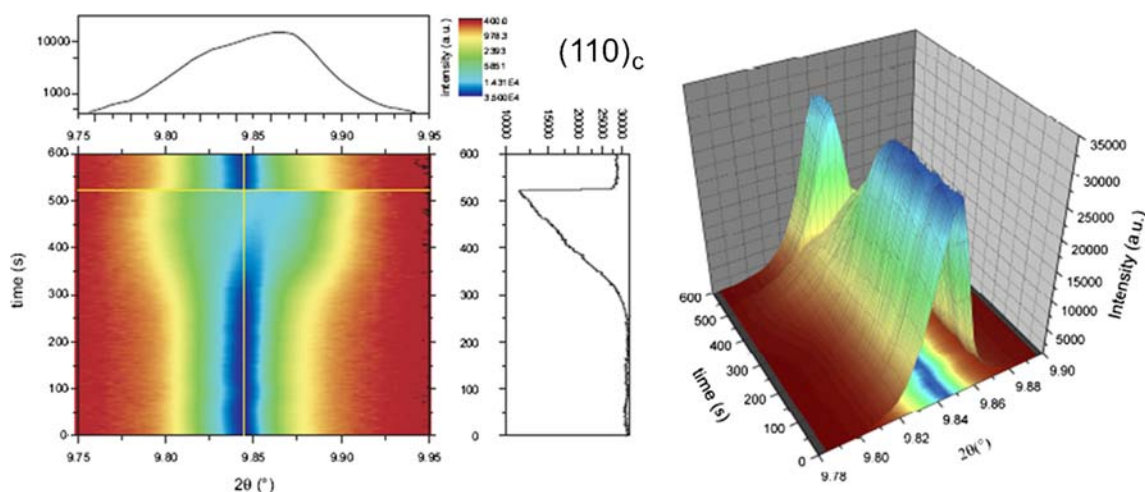


**Fig. 12** Contour and perspective image of electric-field-dependent X-ray diffraction on 0.92BNT-0.06BT-0.02KNN [59]. The cross sectional images indicated by yellow lines in the contour plot are shown on the top and right

0.07BT, one of the alleged MPB compositions, is indeed cubic but transforms into tetragonal when the applied electric field exceeds 3 kV/mm. A systematic investigation on compositionally-homogeneous specimens further revealed that the typically expected MPB feature occurred at 0.89BNT-0.11BT. A series of compositions from 0.95BNT-0.05BT to 0.9BNT-0.1BT displayed cubic symmetry within the resolution limit of the technique used, and all evolved into a phase with non-cubic symmetries on the application of electric field. Compositions with BT content exceeding 12 mol% exhibited normal ferroelectric behavior. Figure 13 summarizes the electric-field-dependent phase stability of BNT-BT. In contrast to previous reports [13, 116–120], even the conventionally known rhombohedral 'ferroelectric' compositions from pure BNT to 0.94BNT-0.04BT [13, 112] were found to undergo a phase transition with not only the lattice parameter but also the degree of lattice distortion changing before and after electrical poling. This was further verified by electric-field-induced volume change measurements that revealed the presence of a remanent volume after electric poling, an indication for electric-field-induced phase transition [68].

In fact, the assumption that the BNT-BT-(KNN) system is a relaxor ferroelectric is strongly supported by the temperature-dependent dielectric permittivity data of unpoled specimens. Figure 14 exemplarily presents the temperature-dependent dielectric permittivity of 0.94BNT-0.06BT. A frequency-dependent dielectric dispersion, which is considered to be one of the most decisive features in relaxor ferroelectrics [108, 121, 122], is apparent at room temperature. Nevertheless, many different interpretations have been proposed in the literature partly due to the unusual shape profile, i.e., two successive dielectric anomalies, and partly due to the presumed existence of antiferroelectricity in-between the two dielectric anomalies [123–129]. Here, it should be pointed out that the designation
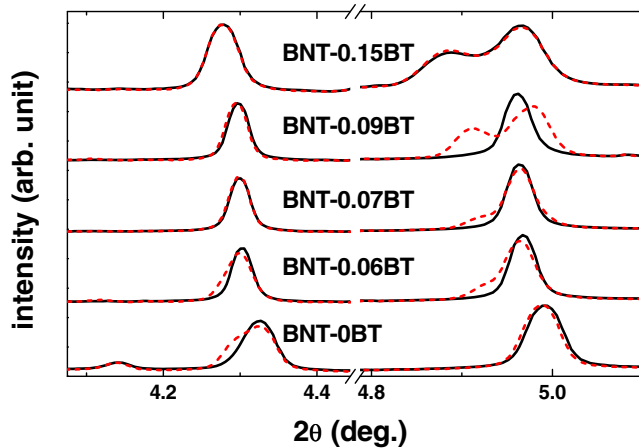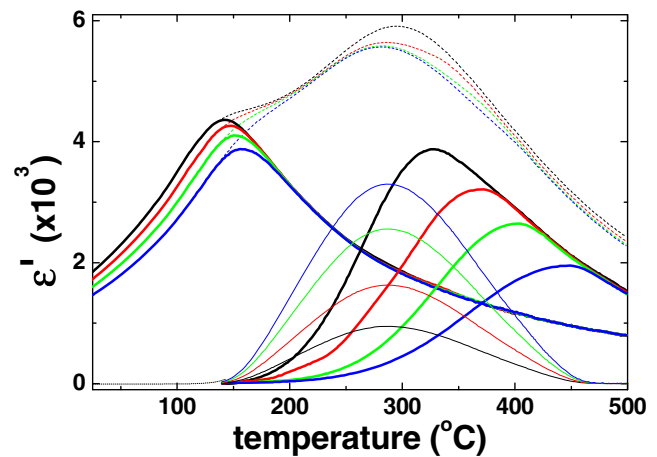


Fig. 14 Temperature-dependent dielectric permittivity of unpoled 0.94BNT-0.06BT (broken lines). The featured two successive dielectric anomalies, one at ~130 °C and the other at ~300 °C, were interpreted as a convolution of three distinct processes, dielectric relaxation due to a mixture of two different types of PNRs of competitive free energy, diffuse phase transition of lower symmetry PNRs into higher symmetry PNRs, and additional dielectric relaxation of existing PNRs [18].

of antiferroelectricity is merely based on the observation of polarization double hysteresis [125] that can originate from many different reasons as discussed in the previous section.

As a reminder, the giant strain in the BNT-BT-KNN system was first discovered during replacement of BNT in 0.94BNT-0.06BT with KNN. Figure 15 provides the polarization and strain hysteresis of three compositions in the (1-$x$)BNT-0.06BT-$x$KNN system during the bipolar poling cycle. As mentioned earlier, the birth of giant strain is accompanied by a significant constriction in the polarization hysteresis, and the extent of the achieved strain level is closely related to a rapid decrease in $S_{rem}$. Little contribution of electric-field-induced volume change is denoted as the volume change is independent on composition. In addition, the radial strain is seen to mirror the axial strain with the magnitude being negative at all time.

A set of temperature-dependent hysteresis measurements on 0.93BNT-0.06BT-0.01KNN given in Fig. 16(a) confirms that the changes induced by compositional modifications are apparently identical with those encountered during thermal evolution of a composition with a butterfly-shaped strain characteristic. As expected, constriction tends to develop in the polarization hysteresis loop, leading to a double-like hysteresis loop with increasing temperature. In the meantime, both $S_{rem}$'s in axial and radial strain decrease rapidly to zero, giving rise to a giant strain. Here, two points are worth attending to. The total amount of volume change during cycling does not change with measurement temperature, which again confirms that the observed giant strain is not related to electric-field-induced volume change. As well, the pinching in the polarization hysteresis starts to develop slightly below the ferroelectric-to-relaxor transition temperature



Fig. 13 X-ray diffraction patterns of selected compositions in BNT-BT system showing (111)pc and (200)pc [224]. The solid black lines and broken red lines refer to the diffraction patterns collected in situ at 0 kV/mm and at 6 kV/mm, respectively
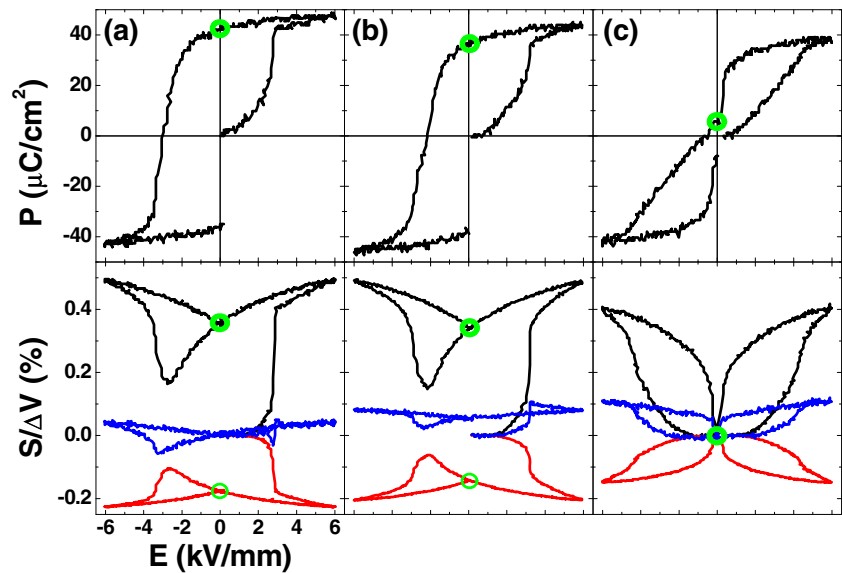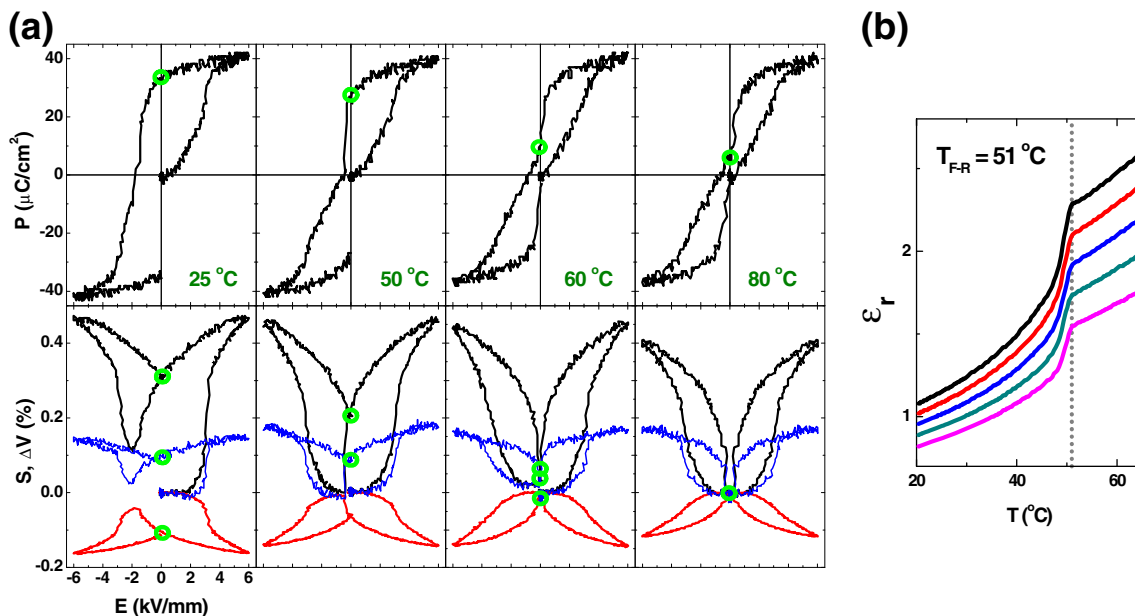
**Fig. 15** Polarization and strain hysteresis with the concurrent volume changes in (**a**) 0.94BNT-0.06BT, (**b**) 0.93BNT-0.06BT-0.01KNN, and (**c**) 0.91BNT-0.06BT-0.03KNN. All the samples were sintered at 1150 °C for 3 h



($T_{F-R}$), which can be estimated by the frequency-independent discontinuity in the temperature-dependent dielectric permittivity or dissipation factor measured on poled specimens [18, 82]. Note that $T_{F-R}$ determined by dielectric permittivity measurement is often about several degrees higher than the actual depolarization temperature ($T_d$) [104, 130], which will be further discussed in the next section. $T_{F-R}$ determined by the dielectric permittivity measurement for 0.93BNT-0.06BT-0.01KNN is 51 °C (Fig. 16(b)).

The BNT-BT-KNN system is contrasted to a relaxor ferroelectric material with emphasis on temperature-dependent hysteresis loops. To this end, we chose a commercially available hot-pressed PLZT 8/65/35 relaxor, the $T_{F-R}$ of which is at

34 °C according to dielectric permittivity measurement [18]. Figure 17(a) displays thermal evolution of polarization hysteresis and a set of strain hysteresis during a bipolar poling cycle. Similar to 0.93BNT-0.06BT-0.01KNN, the polarization hysteresis loop starts to be constricted approaching $T_{F-R}$ and evolves into a double-like hysteresis beyond $T_{F-R}$. In the meantime, the strain hysteresis below $T_{F-R}$ resembles that of normal ferroelectric materials with $S_{rem}$ and $S_{neg}$. The thermal evolution of both polarization and strain hysteresis loops is consistent with the previous observation by Rauls et al. [131] for the same composition. An additional feature revealed in the current experiment is the radial strain that is negative at all time, mirroring the axial one. When temperature is increased



**Fig. 16** (**a**) Temperature-dependent polarization and corresponding strain hysteresis with volume change of 0.93BNT-0.06BT-0.01KNN. (**b**) Temperature-dependent dielectric permittivity near $T_{F-R}$
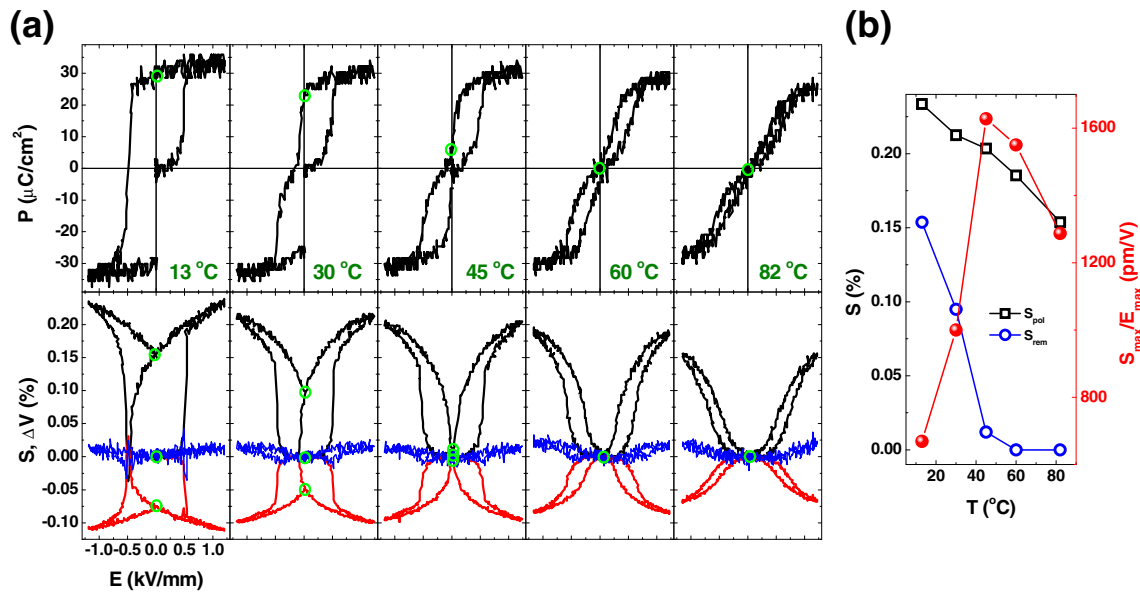
**Fig. 17** Temperature-dependent polarization and corresponding strain hysteresis of a commercial relaxor ferroelectric, $(Pb_{0.92}La_{0.08})(Zr_{0.65}Ti_{0.35})$ $O_3$ (PLZT 8/65/35, Boston Applied Technology, MA). $T_{F-R}$ from the dielectric permittivity measurement is at 34 °C [18].

further, $S_{rem}$ starts to decrease sharply, and vanishes through $T_{F-R}$, resulting in a significant increase in $S_{max}/E_{max}$ that decreases gradually with further increase in temperature. Comparably good temperature stability of giant strain in relaxor in comparison to paraelectric materials such as BT above the Curie point can be attributed to the presence of polar nanoregions (PNRs) that reduces the energy barrier for the nucleation of ferroelectric order on the application of electric field. Note that the changes in $S_{max}$, $S_{rem}$, and the corresponding $S_{max}/E_{max}$ summarized in Fig. 17(b) bear close resemblance to those of 0.93BNT-0.06BT-0.01KNN in Fig. 10(b). In fact, this enhanced strain behavior was already demonstrated in another representative relaxor perovskite, $Pb(Mg_{1/3}Nb_{2/3})O_3$ (PMN), in as early as 1994 (Fig. 18). Little attention was paid to the giant strain at the time possibly because the temperature where the giant strain was induced was too low for practical applications [132]. The changes in the $S_{pol}$, $S_{rem}$, and $S_{max}/E_{max}$ with temperature again resemble those both of PLZT 8/65/35 and 0.93BNT-0.06BT-0.01KNN. In addition, the total volume

change during cycling remains invariant to temperature change as in 0.93BNT-0.06BT-0.01KNN. The comparison of the two representative perovskite relaxors, PLZT 8/65/35 and PMN, with BNT-BT-KNN strongly indicates that 0.93BNT-0.06BT-0.01KNN should be classified as a relaxor ferroelectric and the giant strain is inherent to the relaxor characteristics.

### 3.3 Mechanistic understanding and phase identity of the BNT-BT-(KNN) system

As discussed so far, the $(1-x)$BNT-0.06BT-$x$KNN system belongs to the relaxor ferroelectric category. It should be emphasized that this holds true not only for the compositions with giant strain but also for those conventionally considered ferroelectric compositions such as 0.94BNT-0.06BT. However, it is apparent that the compositions with negligible $S_{rem}$ that results in a giant strain are clearly distinguished from those with a sizable $S_{rem}$ such as 0.94BNT-0.06BT. The former undergoes a reversible phase transformation on the

**Fig. 18** Temperature-dependent poling strain of PMN (left) and the changes in key parameters defining strain characteristic as a function of temperature (right) [132].
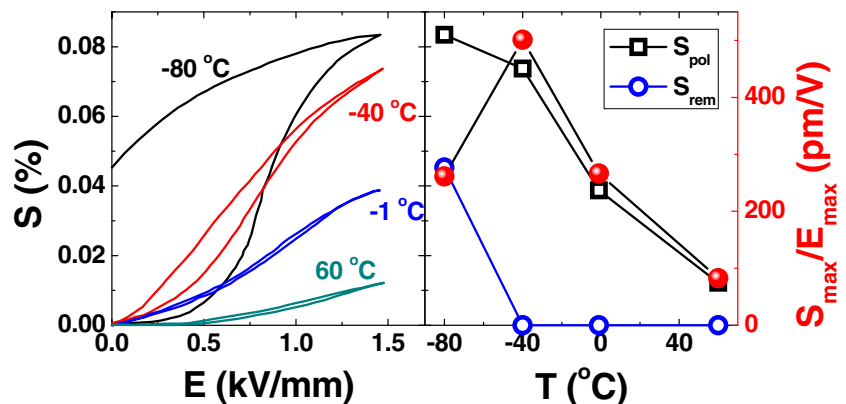
application of electric field, while the latter does an irreversible one. Then, the natural question is, 'What makes the difference in the kinetics of the electric-field-induced phase transformation?' The answer to the question can be found in the literature on relaxor ferroelectrics.

When the first archetypal perovskite relaxor, PMN, was discovered by Smolenskii and his colleagues in the early 1960's, the material was believed to be ferroelectric with the Curie point smeared out due to chemical inhomogeneity, resulting in a multitude of local first order phase transition temperatures, which has usually been referred to as diffuse phase transition (DPT) model [133, 134]. The assignment of ferroelectricity was justified by the well-developed square polarization hysteresis loop below room temperature. In spite of the phenomenological plausibility, the DPT model was soon discarded, because the DPT is frequently observed also in many non-relaxor ferroelectrics [135]. Later, it was shown that the relaxor behavior is only a matter of scale of microstructural inhomogeneity evidenced by the observation of short-range chemical order at nanoscales [136]. Cross [108] proposed a superparaelectric model by the analogy with superparamagnetism, attributing the relaxor behavior to the presence of dynamic nanoscale dipolar clusters thermally fluctuating among the equivalent polarization states. On the basis of the observation that the activation energy for the polarization fluctuation does not follow the simple Arrhenius relation but the Vogel-Fulcher relation, the superparaelectric model was soon refined into the polar-glassy model stating that there exists a static freezing temperature due to a frustrated correlation among thermally fluctuating superparaelectric moments [135]. The significance of the polar-glassy model can be found in the fact that it predicts two different types of relaxor states, non-ergodic and ergodic relaxor state. Later, it was proposed that the predicted freezing state should consist of nanosized domains, the formation of which is due to quenched random electric fields, and its validity was evidenced by Barkhausen jumps during poling of non-ergodic relaxor PMN [137]. This random field model clearly explains why an externally applied electric field gives birth to ferroelectric order out of a non-ergodic relaxor state. In addition, the relaxation process even in the ergodic relaxor state was further proposed being related to domain-type dynamics from an observation of a strong nonlinearity in the frequency dispersion of dielectric signals [138]. Several advanced models giving further insight into relaxor phenomena have been introduced so far in the literature such as random-site model [139], spherical-random-bond-random-field model [140], *etc*. The state of the art in the contemporary understanding of relaxor ferroelectrics is readily available in several excellent review articles [121, 122, 141]. Within the scope of the current contribution, the most important information to be noted is that relaxors can have two different states. One transforms irreversibly into the ferroelectric state (non-ergodic relaxor) and the other one does reversibly (ergodic relaxor).

As detailed by Viehland et al. [135], the reciprocal of the temperature for the maximum dielectric permittivity ($T_{max}$) asymptotically approaches a value, which is termed freezing temperature ($T_f$), when measurement frequency approaches zero. Hence, one can easily imagine that changes in temperature of a couple of degrees around $T_f$ result in a drastic change in the kinetics of polar entities in relaxors. By definition, $T_f$ is the $T_{max}$ of the static dielectric permittivity, *i.e.*, the dielectric permittivity measured at 0 Hz. Therefore, $T_f$ can be estimated from frequency-dependent dielectric permittivity data recorded while cooling at a constant cooling rate by a numerical fit using Vogel-Fulcher relationship in analogy to glass transition. However, this method requires a wider range of frequencies than the commonly-selected frequencies from 100 Hz to 1 MHz with an exponentially increasing interval. It is noted that the Vogel-Fulcher equation has three unknown parameters to be fitted. In addition, one of the practical implications of the presence of $T_f$ stems from the fact that it confines the upper temperature limit for piezoelectric applications, because the materials lose their macroscopic poling state above $T_f$ [142]. Instead of $T_f$, therefore, $T_{F-R}$ or $T_d$ that is by far easier to determine suffices for most practical situations. In fact, it was already shown that the depolarization process represented by $T_d$ shares a common origin with $T_f$ [135, 142–144].

Although, in principle, $T_d$ is the temperature at which pyroelectric current peaks, *i.e.*, at the inflection point in the associated decaying remanent polarization curve [104, 130], $T_{F-R}$ is often reported as $T_d$ alternatively from temperature-dependent dielectric permittivity measurements on poled specimens [116–119, 145]. However, identifying $T_{F-R}$ with $T_d$ requires caution, because they often differ from each other significantly. This is especially true when depolarization takes place over a range of temperatures, which is the case for BNT-based materials [146, 147]. Figure 19(a) provides the temperature-dependent dielectric permittivity of poled PLZT 8/65/35 in comparison to the changes in remanent polarization derived from thermally induced depolarization current measurements. The sharp change in $P_{rem}$ suggests that the depolarization of PLZT 8/65/35 takes place abruptly at ~34 °C, where the dielectric permittivity curve becomes singular, which is fairly consistent with literature [135, 142, 143]. In contrast, however, it is interesting to note that the rate of decreasing $P_{rem}$ is much smaller in 0.94BNT-0.06BT than in PLZT 8/65/35; thus, $T_d$ deviates significantly from the dielectric anomaly as shown in Fig. 19(b). This deviation was rationalized in our previous contributions by assuming two successive depolarization processes, *i.e.*, domain randomization followed by break-up of ferroelectric domains into PNRs [104, 130].

The discussion so far allows us to conclude that not only 0.92BNT-0.06BT-0.02KNN but also 0.94BNT-0.06BT that has been conventionally considered as a normal ferroelectric

**Fig. 19** Comparison of depolarization temperature ($T_d$) measured by temperature-dependent dielectric permittivity and remanent polarization estimated by thermally stimulated depolarization current for **(a)** PLZT 8/65/35 and **(b)** 0.94BNT-0.06BT. The measurement frequency for the dielectric signals is 0.1, 1, 10, and 100 kHz sequentially in the order of magnitude with the largest dielectric response at 100 Hz
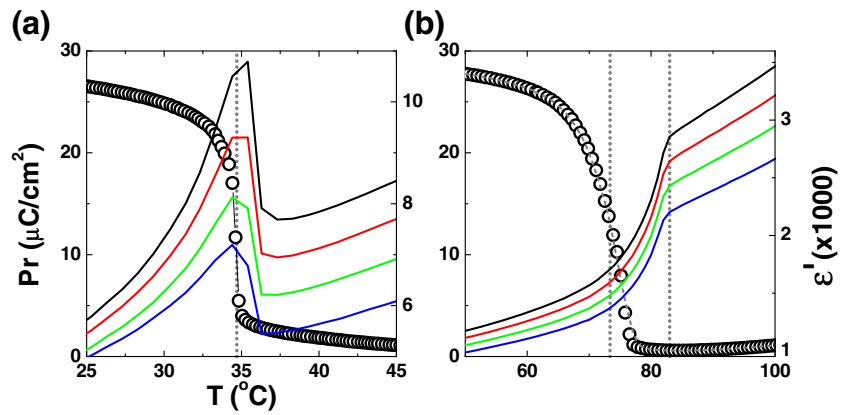


phase are both relaxors as long as the phase is not disturbed by externally applied electric fields. As summarized in Fig. 20, 0.94BNT-0.06BT is a non-ergodic relaxor, which transforms irreversibly into a ferroelectric phase upon the application of a sufficiently large electric field. This irreversibility in the electric-field-induced phase transition can be rationalized by sluggish kinetics of a randomizing effect imposed by random fields. The electric-field-enforced ferroelectric phase persists as long as the material resides below $T_d$. On the other hand, it is evident that the role of the addition of KNN into the BNT-BT system is to reduce both $T_d$ and $T_{F-R}$, and the giant strain appears when the $T_{F-R}$ shifts down slightly below room temperature [147]. In this case, since the material is an ergodic relaxor at room temperature, the application of sufficiently large electric fields can reversibly induce ferroelectric long range order, which is only stable under electric field. It was recently proposed that the origin of the loss of non-ergodicity in BNT-based materials be related to the breaking of Bi-O hybridization that promotes a long-range non-cubicity in the system [148].
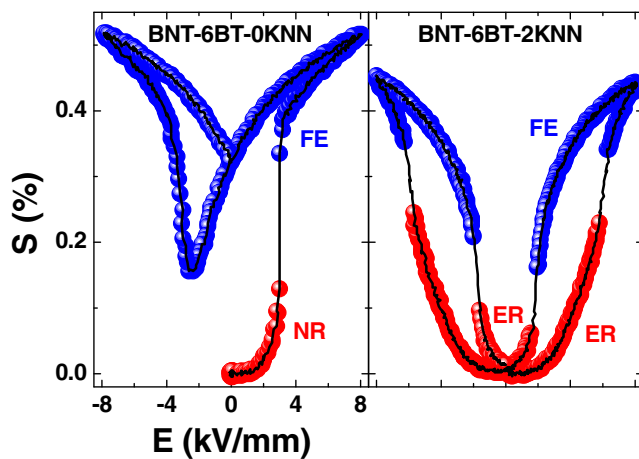


**Fig. 20** The identity of the electric-field-induced phase transition observed in 0.94BNT-0.06BT (left) and 0.02BNT-0.06BT-0.02KNN (right). FE, NR, and ER denote ferroelectric, non-ergodic relaxor, and ergodic relaxor phase, respectively

## 4 Achieved normalized strains

Large signal electric-field-induced strain behavior of various BNT-based material systems has been extensively studied over the last 6 years, which amounts to about 10 % of the entire publications over the same period (See for example Fig. 2).

Hiruma et al. [149] introduced $SrTiO_3$ (ST) to BNT and found that the initially existing $R3c$ rhombohedral distortion gradually vanished as the concentration of ST reached 28 mol%, resulting in a 'cubic' structure. Consistent with literature [43–45, 57, 65], they also observed that the appearance of cubic symmetry was accompanied by a rapid decrease in $d_{33}$, while typical butterfly-shaped strain hysteresis loops transform into sprout-shaped ones with little negative strain. Soon after, they also reported chemically-induced giant strains in BNT-KNbO$_3$ (KN) [150], BNT-Bi(Al$_{1/2}$Nb$_{1/2}$)O$_3$ (BAN) [151], and BNT-Bi(Al$_{1/2}$Sb$_{1/2}$)O$_3$ (BAS) [152]. Later, the effect of ST into BNT on the electric-field-induced strains was confirmed by Krauss et al. [153], who reported a giant strain behavior at 25 mol% ST. On the other hand, Zuo et al. [154] showed that a substitution of Ta$^{5+}$ for Ti$^{4+}$ in the BNT-BT system also gives birth to a giant strain, implying that the major origin of the previously reported KNN-induced giant strain in 0.94BNT-0.06BT [43] could be due to the substitution of Nb$^{5+}$ for Ti$^{4+}$. This is, indeed, reasonable in that additional substitution of Nb$^{5+}$ as a donor tends to destabilize ferroelectric order in BNT-BT-KNN system, while the acceptor doping resulted in a counter-effect [155]. This counter-effect was further verified in a CuO-added 0.92BNT-0.06BT-0.02KNN [156]. In the meantime, attention has been paid also to the solid solutions based on BNT-BKT-based system [157–163]. The appearance of giant strains in the BNT-BKT-based system was demonstrated to phenomenologically follow the same mechanism as in the BNT-BT-based system.

Figure 21 summarizes unipolar strains of selected compositions in comparison with commercial soft PZT, PIC151 and the textured KNN ceramic. A couple of significant achievements are noted. The electric field required to trigger giant strains is reduced to a level that allows $S_{max}/E_{max}$ to
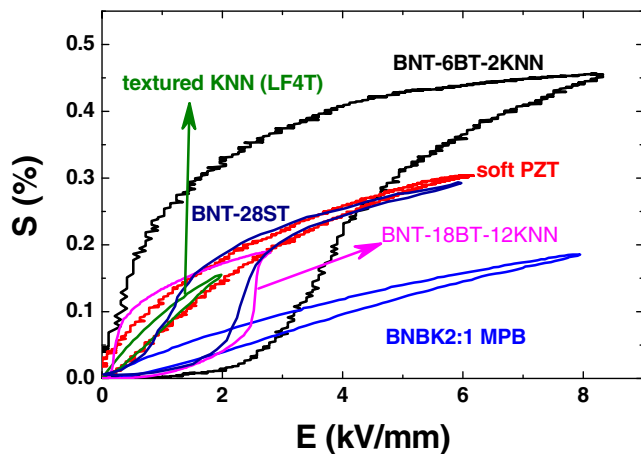
**Fig. 21** State of the art of the electric-field-induced strains in comparison with that of soft PZT (PIC151). It is noted that above the electric field level of 3 kV/mm, the achievable strains in 0.72BNT-0.28ST [149] and 0.704BNT-0.176BT-0.12KNN [225] are highly competitive to that of soft PZT

reach in excess of 600 pm/V at electric fields of as low as 3 kV/mm. As well, large hysteresis due to switching processes in induced-ferroelectric order is also notably suppressed. A summary of relevant parameters from all the discussed materials is given in Table 1.

## 5 Further considerations for practical applications

So far, we have only considered the maximum achievable strains in BNT-based systems. Although $S_{max}/E_{max}$ is one of the most important parameters to be considered for actuator applications, there are several more parameters to be considered. Although currently reported strain properties of piezoceramics are confined to relatively slow driving frequencies in the vicinity of 1 Hz, the driving frequencies for real applications easily exceed kHz level. Especially in the case of ultrasonic motors that are driven at resonance frequency, the driving frequency lies in the range of tens to hundreds of kHz. Next to the dependence of strains on driving frequency, long-term stability represented by fatigue characteristics and the blocking stress as the ability to overcome the stress imposed by a preloading component in practical devices are important characteristics.

### 5.1 Frequency dependence

Figure 22 displays the frequency dependence of the electric-field-induced strains of lead-free materials in comparison with the commercial soft PZT, PIC151. It is well-known that increasing driving frequencies hinder ferroelectric domains from switching, leading to a linear increase in the coercive field as the measurement frequency increases logarithmically

**Table 1** A summary of actuating performance of reported materials. To save the space, the composition of each material is simplified as follows: $0.72BNT-0.28SrTiO_3$ as BNT-28ST [149], $0.92BNT-0.08KNbO_3$ as BNT-8KN [150], $0.945BNT-0.055Ba(Al_{1/2}Nb_{1/2})O_3$ as BNT-5.5BAN [151], $0.955BNT-0.045Ba(Al_{1/2}Sb_{1/2})O_3$ as BNT-4.5BAS [152], $([Bi_{1/2}Na_{1/2}]_{0.94}Ba_{0.06})(Ti_{0.98}Ta_{0.02})O_3$ as BNT-BT-2Ta [154], $0.92BNT-0.06BT-0.02KNN$ as BNT-BT-2KNN [44], $Bi_{1/2}(Na_{0.78}K_{0.22})_{1/2}(Ti_{0.97}Hf_{0.03})O_3$ as BNKT-3Hf [158], $Bi_{1/2}(Na_{0.82}K_{0.18})_{1/2}(Ti_{0.97}Nb_{0.03})O_3$ as BNKT-3Nb [160], $Bi_{1/2}(Na_{0.78}K_{0.22})_{1/2}(Ti_{0.97}Zr_{0.03})O_3$ as BNKT-3Zr [157], $0.97(Bi_{1/2}(Na_{0.78}K_{0.22})_{1/2}TiO_3)-0.03BiAlO_3$ as BNKT-3BA [162], $0.99(0.8BNT-0.2[Bi_{1/2}K_{1/2}]TiO_3)-0.01(0.97 KNN-0.03[Bi_{1/2}K_{1/2}]TiO_3)$ as BNKT-1KNN [161], and $(Bi_{0.5}Na_{0.385}K_{0.09}Li_{0.025})(Ti_{0.975}Ta_{0.025})O_3$ as BNKT-2.5Li2.5Ta [159]

| Material | $E_{pol}$ (kV/mm) | $S_{max}/E_{max}$ at $E_{pol}$ (pm/V) | $S_{max}/E_{max}$ at 4 kV/mm (pm/V) | Frequency (mHz) |
|---|---|---|---|---|
| BNT-28ST | 2.33 | 515 | 600 | 100 |
| BNT-8KN | 5.31 | 508 | 275 | 100 |
| BNT-5.5BAN | 5.57 | 413 | 200 | 100 |
| BNT-4.5BAS | 5.69 | 369 | 125 | 100 |
| BNT-BT-2Ta | 4.81 | 270 | 200 | 300 |
| BNT-BT-2KNN | 3.59 | 418 | 575 | 50 |
| BNKT-3Hf | 4.15 | 337 | 325 | 300 |
| BNKT-3Nb | 4.71 | 488 | 325 | N/A |
| BNKT-3Zr | 3.93 | 509 | 525 | 300 |
| BNKT-3BA | 3.89 | 411 | 425 | N/A |
| BNKT-1KNN | 4.93 | 406 | 225 | 100 |
| BNKT-2.5Li2.5Ta | 4.11 | 414 | 350 | N/A |

[164–166]. Figure 22(a) demonstrates that one of the consequences of this hindered domain switching in PZT is a linear decrease in the maximum strain level with logarithmically increasing frequency. PZT loses ~27 pm/V in $S_{max}/E_{max}$ (0.0053 % strain at 2 kV/mm) for every 10-fold increase in frequency up to 100 Hz, corresponding to ~0.5 % degradation in $S_{max}/E_{max}$ with a reference to $S_{max}/E_{max}$ at 50 mHz.

On the other hand, the absolute decrease in the achievable strain level in 0.92BNT-0.06BT-0.02KNN appears more pronounced at 0.029 % for every 10-fold increase in frequency, which is about ~5 times larger than that of PZT (Fig. 22(b)). However, it should be noticed that the corresponding degradation in the actuating performance in terms of normalized strain is more or less similar to that of PZT at ~36 pm/V that leads to ~7 % decrease in $S_{max}/E_{max}$ for every 10-fold increase in frequency with a reference to $S_{max}/E_{max}$ at 50 mHz. It follows that the performance at 100 Hz is at most three quarters of that at 50 mHz. In analogy with the aforementioned mechanism for normal ferroelectrics involving the increase in the coercive field, the frequency-dependent degradation in the giant strain can be related to the increase in the inflection point during uphill cycle where the initial ergodic relaxor phase is expected to transform into a ferroelectric phase [50, 155, 167]. As demonstrated by a continuous
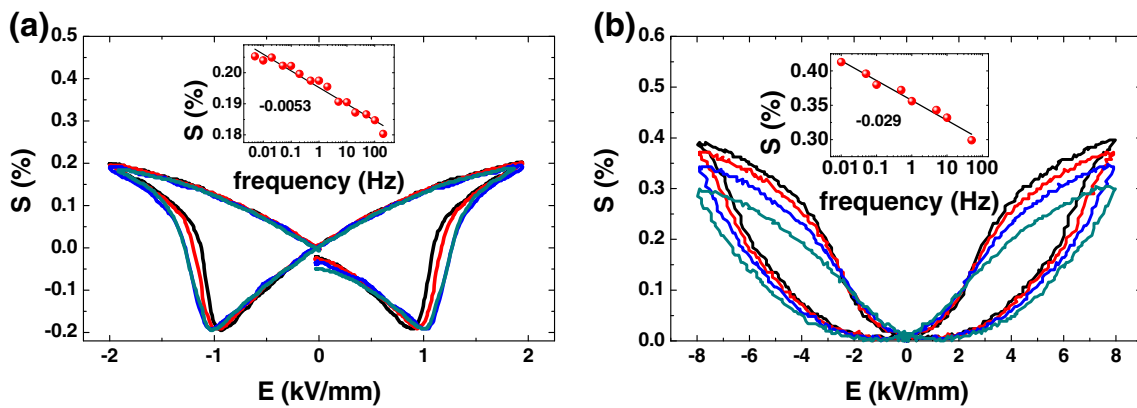
**Fig. 22** Electric-field-induced strains of (**a**) PIC151 and (**b**) 0.92BNT-0.06BT-0.02KNN at different driving frequencies. The measurement frequencies for each plot are 50 mHz, 500 mHz, 5 Hz, and 50 Hz from top to bottom. All the inset figures show that the electric-field-induced unipolar strain decreases linearly with increasing measurement frequencies in a logarithmic scale. The presented number in each inset figure is the slope from a linear fitting

electrical cycling with offsets, the inflection point during the uphill and downhill cycle represents the relaxor-to-ferroelectric transition field ($E_{R-F}$) and ferroelectric-to-relaxor transition field ($E_{F-R}$), respectively [155]. Hence, the fact that both $E_{R-F}$ and $E_{F-R}$ tend to increase with increasing frequency implies that the measurement frequency has a strong influence on the phase transition kinetics.

## 5.2 Fatigue characteristics

Electrical fatigue had been studied in lead-containing materials for about 20 years, and was summarized into a review paper for bulk PZT some years ago [168]. The following phenomena can occur during the fatigue process:

a) Microcracks and macrocracks
b) Changes to crystal structure and microstructure
c) Charge redistribution.

So far, only few studies on lead-free electro-strain ceramics have been published [169–172]. For BNT-based ceramics, it was noted that 0.94BNT-0.06BT is very sensitive to both unipolar as well as bipolar fatigue loading due to changes in crystal structure leading to microcracking [170]. In contrast,

Cu-doping rendered the initial structure stable and only little fatigue degradation was noted [169]. Materials with giant strain finally exhibited almost no quantifiable degradation even with fatigue loading at 6 kV/mm and 0.37 % strain for $10^6$ cycles (Fig. 23) [171]. This result is exemplified by contrasting the bipolar strain hysteresis for 0.93BNT-0.06BNT-0.01KNN (still depicting butterfly hysteresis of ferroelectrics) with 0.91BNT-0.06BT-0.03KNN where the ferroelectric order develops with every new cycle and the loops after $10^6$ cycles can almost not be distinguished from the first loop [171].

## 5.3 Blocking stress

In actuator applications, work is required to be performed against an external force [173, 174]. Therefore, free stroke, *i.e.*, the stroke under zero-stress conditions, is not suited to comprehensively characterize the performance of actuators. Just as important as the maximum stroke is the maximum force that can be harvested under a specific electric field. This force is termed blocking force, which is defined as the maximum force an actuator can generate against an infinitely stiff external clamping [175]. Technically, blocking force

**Fig. 23** Bipolar strain hysteresis of (**a**) 0.93BNT-0.06BT-0.01KNN and (**b**) 0.91BNT-0.06BT-0.03KNN. The cycle number for each curve is 1, $10^4$, and $10^6$ from top to bottom [171].
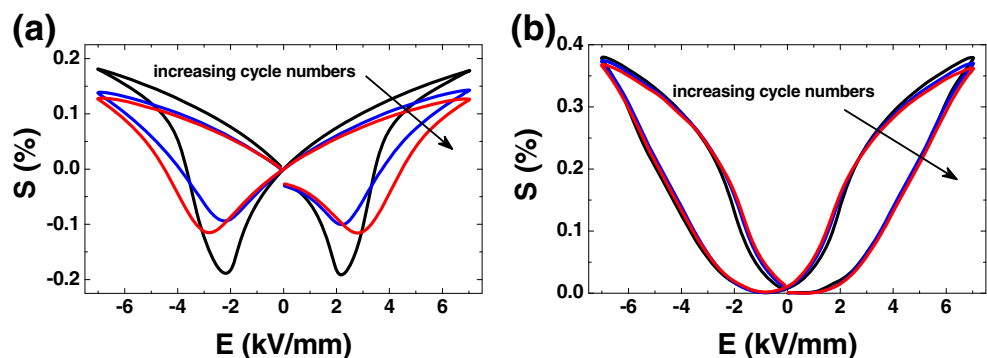
is measured by compressing a sample which is freely elongated by means of an applied electric field, whereas blocking force is determined by the force where the force-stroke-curve intersects with the axis of ordinate. While the stroke and blocking force are important parameters for the final actuator, it is more convenient to use blocking stress ($\sigma_B$) and free strain ($S_f$) in comparing different materials, since they are geometry independent. Stress–strain curves allow computation of the specific work $w$, which is the work that is performed per volume, according to the following formula.
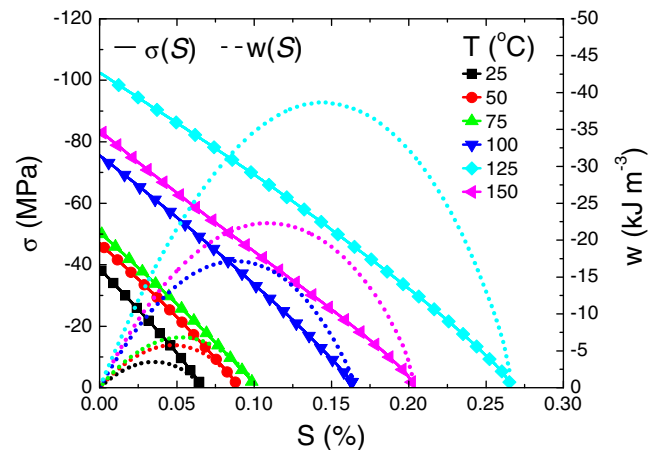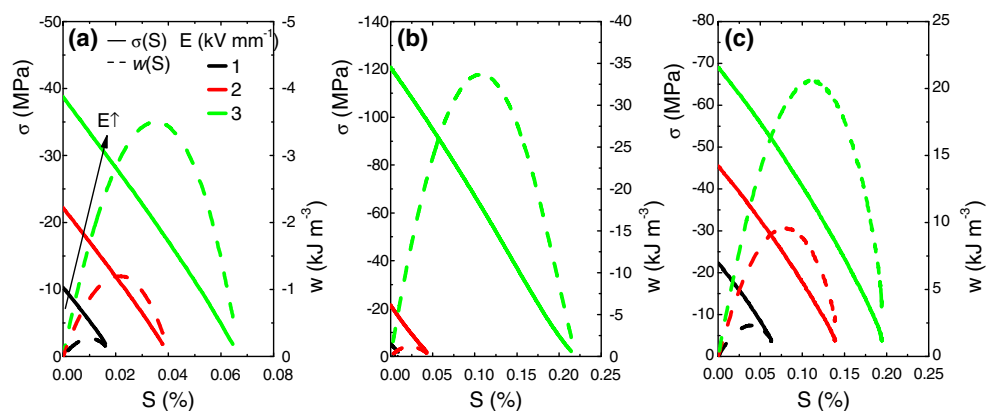
$$w = 0.5 \cdot \sigma \cdot S \tag{8}$$

Since there should be no work performed by actuators when they are completely blocked ($S$=0) or completely unstrained ($\sigma$=0), the maximum specific work ($w_{max}$) lying between the two extreme cases is a figure of merit that characterizes how much mechanical work an actuator can provide under optimum, matched conditions. Further detailed information on the topic can be found in Ref. [176].

Stress-dependent polarization hysteresis measurements by Tan et al. [146] gave early indication that BNT-based lead-free piezoceramics may provide high blocking stresses, which was later confirmed by Dittmer et al. [177]. Figure 24 presents the stress–strain curves for 0.94BNT-0.06BT, 0.92BNT-0.06BT-0.02KNN, and soft PZT (PIC151) at room temperature for three different electric-field levels such as 1 kV/mm, 2 kV/mm and 3 kV/mm. The electric-field-induced $S_f$ of 0.94BNT-0.06BT (Fig. 24(a)) amounts to about one third of $S_f$ in soft PZT (Fig. 24(c)). Even with the increased stiffness of the BNT-BT material [177], $\sigma_B$ of 0.94BNT-0.06BT (39 MPa) is smaller than in PZT (69 MPa) and the maximum specific work ($w_{max}$) is significantly smaller at 3.5 kJ/m³ compared to 21 kJ/m³ in PZT. However, it is noted that $\sigma_B$ of 0.92BNT-0.06BT-0.02KNN is 1.8 times larger at 124 MPa than that of PZT for the same magnitude of driving field; hence, $w_{max}$ is also larger at 34 kJ/m³.

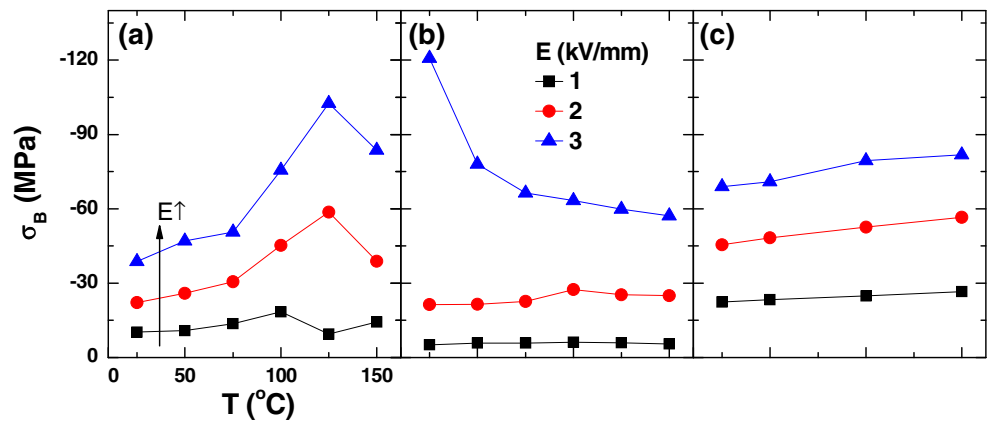Temperature dependence of the blocking stress is another salient issue [178, 179]. Compared to PZT, the temperature



**Fig. 25** Stress $\sigma$ (solid line) and specific work $w$ (dotted line) plotted against strain $S$ for 0.94BNT-0.06BT at 3 kV/mm for various temperatures ranging from 25 °C to 150 °C

dependence of the blocking stress is more pronounced and nonlinear for 0.94BNT-0.06BT as depicted in Fig. 25. This is due to the fact that the electric-field-induced strain is highly temperature-sensitive [57]; therefore, the resulting blocking stress likewise depends on temperature with a maximum $\sigma_B$ of 102 MPa at 125 °C and $w_{max}$ of 39 kJ/m³ for 3 kV/mm. In the case of 0.92BNT-0.06BT-0.02KNN, a comparable value was already achieved at room temperature as discussed in Fig. 24 (b), but a significant decrease as temperature increases is denoted due to the decrease in the maximum strain value achievable. A summary on the temperature dependence of blocking stress for all the tested materials from room temperature to 150 °C is provided in Fig. 26. The denoted strong temperature dependence of 0.94BNT-0.06BT and 0.92BNT-0.06BT-0.02KNN is, indeed, disadvantageous for applications. However, the remarkably high blocking stresses at distinct peak-temperatures are highly encouraging in that temperature stability of electric-field-induced strain and that of related blocking stress have not yet been tuned for BNT-based materials.

**Fig. 24** Stress $\sigma$ (solid line) and specific work $w$ (dotted line) plotted against strain $S$ for (**a**) 0.94BNT-0.06BT, (**b**) 0.92BNT-0.06BT-0.02KNN, and (**c**) soft PZT PIC151 at room temperature for different driving electric-field levels. Different scales used in each plot should be noted

## 6 Perspectives

The BNT-based systems with giant electric-field-induced strains have a great potential for replacing PZT in the realm of actuator applications, provided that the identified challenges such as relatively large driving electric fields, rather large frequency dependence, temperature stability, *etc.* are sufficiently addressed. Various approaches can be employed to overcome these challenges. Promising pathways are provided by the so-called ceramic/ceramic composite approach and single crystal approach. In this section, we briefly summarize the state of the art of the two issues.

Ceramic/ceramic composites prepared either by blending [180, 181] or layering [182–187] of different materials have been extensively employed during the 1980's and 1990's to optimize the properties and performance of functional electronic materials, specifically dielectrics and ferroelectrics. The reported results on the effect of ceramic/ceramic composites are featured by enhanced temperature stability, enhanced piezoelectricity, and high dielectric stability under high field cycling. This synergic effect induced by the ceramic/ceramic composite approach was interpreted by a series capacitor model based on the rule of mixtures, though the obtained outcomes often deviated from the expected performance predicted by this modeling [188].

Recently, in extension to these earlier works, Lee et al. [189] demonstrated that this composite approach is highly beneficial for best-tailoring the key parameters in optimizing electric-field-induced strain in BNT-based lead-free ceramics. For example, they showed that the electric field required to trigger large strain in BNT-based materials could be significantly lowered with little degradation in the maximum achievable strain level by blending a fraction of non-ergodic relaxor phase (BNT) into ergodic relaxor matrix phase $(0.93Bi_{1/2}(Na_{0.75}K_{0.25})_{1/2}TiO_3\text{-}0.06BiAlO_3)$ as shown in Fig. 27. It is noted that not only the field required for triggering the giant strain but also the maximum level of strain achievable are greatly enhanced. A simplistic explanation to the observed effect can be given by a series capacitor model. It dictates that due to the constant charge constraint at the interfaces, actual electric field applied to the ergodic relaxor should be larger than the externally applied field, which triggers the transition from ergodic relaxor to ferroelectric takes place earlier than it should be. Comparison of the effect on a nearby composition further showed that there exists an optimum volume ratio between non-ergodic matrix and ergodic seed phases; hence, too much seed phase leads to a significant decrease in $S_{max}/E_{max}$ with a strong ferroelectric order. It is also noted that this change induced by the ceramic/ceramic composite approach resembles temperature-induced changes in BNT-based



**Fig. 27** (**a**) Bipolar and (**b**) unipolar strain hysteresis loops of $0.93Bi_{1/2}(Na_{0.75}K_{0.25})_{1/2}TiO_3\text{-}0.06BiAlO_3$ with 0 (0BNT), 10 (10BNT), and 20 vol% (20BNT) BNT
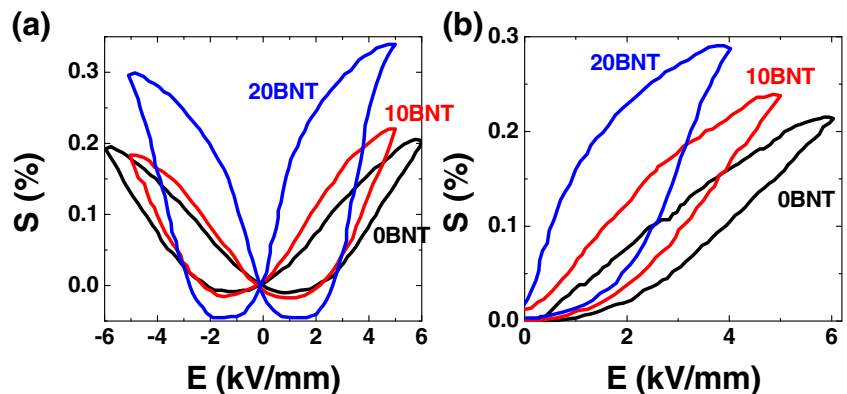
materials [45, 57], meaning that this composite approach is highly effective in tuning the phase stability of BNT-based solid solutions, a possible solution to overcome the still relatively high temperature dependence of functional properties in BNT-based materials.

On the other hand, we know from the history of the development of piezoelectric materials that the success of lead-free incipient piezoelectrics will eventually witness the birth of high quality single crystals [190]. Today's high edge technology has greatly benefited from the advent of high-quality relaxor-based piezoelectric single crystals [191–193], initiated by a historic paper by Park and Shrout in 1997 [194]. The usefulness of single crystals was shown to be further enhanced by a proper domain engineering technique [195]. In fact, the attention to BNT-based materials also, in part, rooted from a success in developing single crystals with giant strains [51, 196]. Attempts to grow lead-free single crystals have already been made in KNN-based [197–201], BNT-based [51, 196, 202–214], and other systems [215, 216] so far. Although excellent and intriguing properties have been reported in the reported lead-free single crystals in the literature, it seems that reported properties and characteristics lack consistency. This inconsistency is highly likely due to the great complexity in the phase diagram. Even the phase diagram of pure BNT system is already quite complicated. So far, only a part of the phase diagram for the ternary $Na_2O\text{-}Bi_2O_3\text{-}TiO_2$ system is available on the $TiO_2$-rich side at 1000 °C [217]. As noted, even in this partial phase diagram, at least four additional Bi-Na-Ti-based oxide compounds including a cubic pyrochlore phase as well as five more other oxide compounds exist as stable phases other than $Bi_{1/2}Na_{1/2}TiO_3$, making the detection of a proper isoplethal path highly challenging. In addition, the task at hand is aggravated by the fact that the functional and structural properties of BNT-based system are highly sensitive to stoichiometry [218–221], which is even harder to control during the fabrication of single crystals. One potentially promising approach to solve this issue may be to utilize solid-state single crystal fabrication method [193, 198, 206, 222], where at least the composition of the final product is reliable. This issue warrants further systematic investigations.

## 7 Summary and conclusions

The world-wide market on piezoelectrics has been robust and is expected to grow steadily bigger. An increase in the research activities initially driven by the environmental regulations such as RoHS tends to show a saturation behavior, but the absolute amount of publications per year is still noteworthy. Among the accumulated achievements in the development of lead-free electrostrain ceramics, we presented a focused review on the electric-field-induced strains in BNT-based lead-free incipient piezoceramics, based on which the mechanism for the recently discovered giant strains in BNT-based materials was discussed in depth. In spite of the addressed challenges such as a rather large frequency- and temperature-dependent degradation in functional properties, the unique features such as tunable complexity in the phases, high-fatigue resistance, large blocking stress, *etc.* were shown to be inherent to BNT-based incipient piezoceramics, which makes them highly competitive candidates for the next generation actuator materials.

## References

1. B. Jaffe, W.R. Cook, H. Jaffe, *Piezoelectric ceramics* (Academic, London, 1971)
2. *Piezoelectric actuators and ultrsonic motors*; *Vol.*, edited by K. Uchino (Kluwer Academic Publishers, Boston, 1997).
3. Off. J. Eur. Union **L167**, 1 (2011).
4. After Robert Bosch GmbH (http://www.bosch-press.com/tbwebdb/bosch-usa/en-US/PressText.cfm?&nh=00&Search=0&id=385)
5. J. Rödel, W. Jo, K.T.P. Seifert, E.-M. Anton, T. Granzow, D. Damjanovic, J. Am. Ceram. Soc. **92**, 1153 (2009)
6. D. Damjanovic, N. Klein, J. Li, V. Porokhonskyy, Funct. Mater. Lett. **3**, 5 (2010)
7. R.-A. Eichel, H. Kungl, Funct. Mater. Lett. **03**, 1 (2010)
8. M.D. Maeder, D. Damjanovic, N. Setter, J. Electroceram. **13**, 385 (2004)
9. P.K. Panda, J. Mater. Sci. **44**, 5049 (2009)
10. T.R. Shrout, S.J. Zhang, J. Electroceram. **19**, 113 (2007)
11. T. Takenaka, H. Nagata, Y. Hiruma, Jpn. J. Appl. Phys. **47**, 3787 (2008)
12. E. Aksel, J.L. Jones, Sensors (Basel) **10**, 1935 (2010)
13. T. Takenaka, K.-I. Maruyama, K. Sakata, Jpn. J. Appl. Phys. **30**, 2236 (1991)
14. M. Ahart, M. Somayazulu, R.E. Cohen, P. Ganesh, P. Dera, H-k Mao, R.J. Hemley, Y. Ren, P. Liermann, Z. Wu, Nature **451**, 545 (2008)
15. D. Damjanovic, Appl. Phys. Lett. **97**, 062906 (2010)
16. Y. Ishibashi, M. Iwata, Jpn. J. Appl. Phys. **37**, L985 (1998)
17. G.A. Rossetti, A.G. Khachaturyan, G. Akcay, Y. Ni, J. Appl. Phys. **103**, 114113 (2008)
18. W. Jo, S. Schaab, E. Sapper, L.A. Schmitt, H.-J. Kleebe, A.J. Bell, J. Rödel, J. Appl. Phys. **110**, 074106 (2011)
19. Y. Saito, H. Takao, T. Tani, T. Nonoyama, K. Takatori, T. Homma, T. Nagaya, M. Nakamura, Nature **432**, 84 (2004)
20. Y. Chang, S.F. Poterala, Z. Yang, S. Trolier-McKinstry, G.L. Messing, Appl. Phys. Lett. **95**, 232905 (2009)
21. Y. Saito, H. Takao, J. Eur. Ceram. Soc. **27**, 4085 (2007)
22. H. Takao, Y. Saito, Y. Aoki, K. Horibuchi, J. Am. Ceram. Soc. **89**, 1951 (2006)
23. E. Fukuchi, T. Kimura, T. Tani, T. Takeuch, Y. Saito, J. Am. Ceram. Soc. **85**, 1461 (2002)
24. T. Kimura, T. Takahashi, T. Tani, Y. Saito, J. Am. Ceram. Soc. **87**, 1424 (2004)

25. D.-S. Lee, S.-J. Jeong, E.-C. Park, J.-S. Song, J. Electroceram. **17**, 505 (2006)
26. Y. Seno, T. Tani, Ferroelectrics **224**, 365 (1999)
27. T. Tani, J. Kor. Phys. Soc. **32**, S1217 (1998)
28. M. Wu, Y. Li, D. Wang, J. Zeng, Q. Yin, J. Electroceram. **22**, 131 (2007)
29. H. Yilmaz, G.L. Messing, S. Trolier-McKinstry, J. Electroceram. **11**, 207 (2003)
30. H. Yilmaz, S. Trolier-McKinstry, G.L. Messing, J. Electroceram **11**, 217 (2003)
31. J.T. Zeng, K.W. Kwok, W.K. Tam, H.Y. Tian, X.P. Jiang, H.L.W. Chan, J. Am. Ceram. Soc. **89**, 3850 (2006)
32. J. Zhao, F. Wang, W. Li, H. Li, D. Zhou, S. Gong, Y. Hu, Q. Fu, J. Appl. Phys. **108**, 073535 (2010)
33. Y. Guo, K.-I. Kakimoto, H. Ohsato, Appl. Phys. Lett. **85**, 4121 (2004)
34. Y. Guo, K.-I. Kakimoto, H. Ohsato, Mater. Lett. **59**, 241 (2005)
35. E. Hollenstein, M. Davis, D. Damjanovic, N. Setter, Appl. Phys. Lett. **87**, 182905 (2005)
36. B. Malič, J. Bernard, J. Holc, D. Jenko, M. Kosec, J. Eur. Ceram. Soc. **25**, 2707 (2005)
37. S. Zhang, R. Xia, T.R. Shrout, G. Zang, J. Wang, J. Appl. Phys. **100**, 104108 (2006)
38. H.-Y. Park, C.-W. Ahn, H.-C. Song, J.-H. Lee, S. Nahm, K. Uchino, H.-G. Lee, H.-J. Lee, Appl. Phys. Lett. **89**, 062906 (2006)
39. Y. Dai, X. Zhang, G. Zhou, Appl. Phys. Lett. **90**, 262903 (2007)
40. N. Marandian Hagh, B. Jadidian, A. Safari, J. Electroceram. **18**, 339 (2007)
41. E.K. Akdoğan, K. Kerman, M. Abazari, A. Safari, Appl. Phys. Lett. **92**, 112908 (2008)
42. K. Wang, J.-F. Li, Adv. Funct. Mater. **20**, 1924 (2010)
43. S.-T. Zhang, A.B. Kounga, E. Aulbach, H. Ehrenberg, J. Rödel, Appl. Phys. Lett. **91**, 112906 (2007)
44. S.-T. Zhang, A.B. Kounga, E. Aulbach, T. Granzow, W. Jo, H.-J. Kleebe, J. Rödel, J. Appl. Phys. **103**, 034107 (2008)
45. S.-T. Zhang, A.B. Kounga, E. Aulbach, W. Jo, T. Granzow, H. Ehrenberg, J. Rödel, J. Appl. Phys. **103**, 034108 (2008)
46. K. Müller, H. Burkard, Phys. Rev. B **19**, 3593 (1979)
47. M.D. Ginsberg, R. Busto, Stroke **29**, 529 (1998)
48. J.R. Rice, J. Mech. Phys. Solids **40**, 239 (1992)
49. H. Iyetomi, P. Vashishta, R.K. Kalia, J. Non-Cryst. Solids **262**, 135 (2000)
50. R. Dittmer, W. Jo, J. Daniels, S. Schaab, J. Rödel, J. Am. Ceram. Soc. **94**, 4283 (2011)
51. Y.M. Chiang, G.W. Farrey, A.N. Soukhojak, Appl. Phys. Lett. **73**, 3683 (1998)
52. E. Sawaguchi, H. Maniwa, S. Hoshino, Phys. Rev. **83**, 1078 (1951)
53. S.-E. Park, M.-J. Pan, K. Markowski, S. Yoshikawa, L.E. Cross, J. Appl. Phys. **82**, 1798 (1997)
54. J.E. Daniels, W. Jo, J. Rödel, V. Honkimäki, J.L. Jones, Acta Mater. **58**, 2103 (2010)
55. J.E. Daniels, W. Jo, J. Rödel, J.L. Jones, Appl. Phys. Lett. **95**, 032904 (2009)
56. R. Ranjan, A. Dviwedi, Solid State Commun. **135**, 394 (2005)
57. W. Jo, T. Granzow, E. Aulbach, J. Rödel, D. Damjanovic, J. Appl. Phys. **105**, 094102 (2009)
58. G.O. Jones, P.A. Thomas, Acta Cryst. B **58**, 168 (2002)
59. M. Hinterstein, M. Knapp, M. Hölzel, W. Jo, A. Cervellino, H. Ehrenberg, H. Fuess, J. Appl. Cryst. **43**, 1314 (2010)
60. J. Kling, X. Tan, W. Jo, H.-J. Kleebe, H. Fuess, J. Rödel, J. Am. Ceram. Soc. **93**, 2452 (2010)
61. A.F. Devonshire, Adv. Phys. **3**, 85 (1954)
62. H.F. Kay, Rep. Prog. Phys. **18**, 230 (1955)
63. R.E. Newnham, V. Sundar, R. Yimnirun, J. Su, Q.M. Zhang, J. Phys. Chem. B **101**, 10141 (1997)

64. A.V. Turik, A.A. Yesis, L.A. Reznitchenko, J. Phys. Condens. Matter **18**, 4839 (2006)
65. S.-T. Zhang, A.B. Kounga, W. Jo, C. Jamin, K. Seifert, T. Granzow, J. Rödel, D. Damjanovic, Adv. Mater. **21**, 4716 (2009)
66. A.B. Kounga, T. Granzow, E. Aulbach, M. Hinterstein, J. Rödel, J. Appl. Phys. **104**, 024116 (2008)
67. D. Damjanovic, Rep. Prog. Phys. **61**, 1267 (1998)
68. W. Jo, J. Rödel, Appl. Phys. Lett. **99**, 042901 (2011)
69. E. Sawaguchi, H. Maniwa, S. Hoshino, Phys. Rev. **83**, 1078 (1951)
70. H. Liu, B. Dkhil, Z. Kristallogr. **226**, 163 (2011)
71. L.E. Cross, Nature **181**, 178 (1958)
72. C.N.W. Darlington, H.D. Megaw, Acta Crystallogr. Sect. B: Struct. Sci. **29**, 2171 (1973)
73. G. Shirane, R. Newnham, R. Pepinsky, Phys. Rev. **96**, 581 (1954)
74. M.H. Francombe, B. Lewis, Acta Cryst. **11**, 175 (1958)
75. D. Fu, M. Endo, H. Taniguchi, T. Taniyama, M. Itoh, Appl. Phys. Lett. **90**, 252907 (2007)
76. C. Kittel, Phys. Rev. **82**, 729 (1951)
77. J. Frederick, X. Tan, W. Jo, J. Am. Ceram. Soc. **94**, 1149 (2011)
78. X. Tan, C. Ma, J. Frederick, S. Beckman, K.G. Webber, J. Am. Ceram. Soc. **94**, 4091 (2011)
79. L. Shebanov, M. Kusnetsov, A. Sternberg, J. Appl. Phys. **76**, 4301 (1994)
80. X. Tan, J. Frederick, C. Ma, W. Jo, J. Rödel, Phys. Rev. Lett. **105**, 255702 (2010)
81. W. Merz, Phys. Rev. **91**, 513 (1953)
82. S. Schaab, T. Granzow, Appl. Phys. Lett. **97**, 132902 (2010)
83. K.G. Webber, Y.-H. Seo, H.-Y. Lee, E. Aulbach, W. Jo, J. Rödel, J. Am. Ceram. Soc. **94**, 2728 (2011)
84. H. Wang, H. Xu, H. Luo, Z. Yin, A.A. Bokov, Z.G. Ye, Appl. Phys. Lett. **87**, 012904 (2005)
85. K. Carl, K.H. Hardtl, Ferroelectrics **17**, 473 (1977)
86. X. Ren, Nat. Mater. **3**, 91 (2004)
87. T. Granzow, E. Suvaci, H. Kungl, M.J. Hoffmann, Appl. Phys. Lett. **89**, 262908 (2006)
88. L.X. Zhang, W. Chen, X. Ren, Appl. Phys. Lett. **85**, 5658 (2004)
89. X.-C. Zheng, G.-P. Zheng, Z. Lin, Z.-Y. Jiang, J. Electroceram. **28**, 20 (2011)
90. Z. Feng, X. Ren, Appl. Phys. Lett. **91**, 032904 (2007)
91. P. J. Stevenson, D. A. Hall, ISAF '96., Proceedings of the Tenth IEEE International Symposium on Applications of Ferroelectrics, East Brunswick, NJ , USA, 313 (IEEE, 1996).
92. G. Arlt, H. Neumann, Ferroelectrics **87**, 109 (1988)
93. D.A. Hall, P.J. Stevenson, Ferroelectrics **187**, 23 (1996)
94. G.H. Jonker, J. Am. Ceram. Soc. **55**, 57 (1972)
95. Y.A. Genenko, J. Glaum, O. Hirsch, H. Kungl, M.J. Hoffmann, T. Granzow, Phys. Rev. B **80**, 224109 (2009)
96. D.C. Lupascu, Y.A. Genenko, N. Balke, J. Am. Ceram. Soc. **89**, 224 (2006)
97. R.-A. Eichel, J. Electroceram. **19**, 11 (2007)
98. M.I. Morozov, D. Damjanovic, J. Appl. Phys. **107**, 034106 (2010)
99. W. Liu, X. Ren, Phys. Rev. Lett. **103**, 257602 (2009)
100. K. Boumchedda, M. Hamadi, G. Fantozzi, J. Eur. Ceram. Soc. **27**, 4169 (2007)
101. L. Burianova, P. Hana, S. Panos, E. Furman, S. Zhang, T.R. Shrout, J. Electroceram. **13**, 443 (2004)
102. C.J. Reilly, J.W. Halloran, E.C.N. Silva, F.M. Espinosa, J. Mater. Sci. **42**, 4810 (2007)
103. D.J. Taylor, D. Damjanovic, A.S. Bhalla, L.E. Cross, J. Mater. Sci. Lett. **10**, 668 (1991)
104. E.-M. Anton, W. Jo, D. Damjanovic, J. Rödel, J. Appl. Phys. **110**, 094108 (2011)
105. Y. Guo, K.-I. Kakimoto, H. Ohsato, Jpn. J. Appl. Phys., Part 1 **43**, 6662 (2004)

106. C.W. Ahn, H.C. Song, S. Nahm, S.H. Park, K. Uchino, S. Priya, H.G. Lee, N.K. Kang, Jpn. J. Appl. Phys., Part 2 **44**, L1361 (2005)

107. L.A. Schmitt, J. Kling, M. Hinterstein, M. Hoelzel, W. Jo, H.-J. Kleebe, H. Fuess, J. Mater. Sci. **46**, 4368 (2011)

108. L.E. Cross, Ferroelectrics **76**, 241 (1987)

109. A. Lebon, H. Dammak, G. Calvarin, J. Phys. Condens. Matter **15**, 3069 (2003)

110. G. Xu, Z. Zhong, Y. Bing, Z.G. Ye, G. Shirane, Nat. Mater. **5**, 134 (2006)

111. F. Cordero, F. Craciun, F. Trequattrini, E. Mercadelli, C. Galassi, Phys. Rev. B **81**, 144124 (2010)

112. Y. Hiruma, Y. Watanabe, H. Nagata, T. Takenaka, Key Eng. Mater. **350**, 93 (2007)

113. C. Ma, X. Tan, J. Am. Ceram. Soc. **94**, 4040 (2011)

114. B. Wylie-van Eerd, D. Damjanovic, N. Klein, N. Setter, J. Trodahl, Phys. Rev. B **82**, 104112 (2010)

115. J. Yao, L. Yan, W. Ge, L. Luo, J. Li, D. Viehland, Phys. Rev. B **83**, 054107 (2011)

116. H. Fan, L. Liu, J. Electroceram. **21**, 300 (2007)

117. Y. Hiruma, H. Nagata, T. Takenaka, Jpn. J. Appl. Phys., Part 1 **45**, 7409 (2006)

118. Y. Makiuchi, R. Aoyagi, Y. Hiruma, H. Nagata, T. Takenaka, Jpn. J. Appl. Phys., Part 1 **44**, 4350 (2005)

119. X.X. Wang, X.G. Tang, H.L.W. Chan, Appl. Phys. Lett. **85**, 91 (2004)

120. G.A. Smolenskii, V.A. Isupov, A.I. Agranovskaya, N.N. Krainik, Sov Phys.-Solid State **2**, 2651 (1961)

121. A.A. Bokov, Z.-G. Ye, J. Mater. Sci. **41**, 31 (2006)

122. G.A. Samara, J. Phys. Condens. Matter **15**, R367 (2003)

123. V. Dorcet, G. Trolliard, P. Boullay, J. Magn. Magn. Mater. **321**, 1758 (2009)

124. V.A. Isupov, Ferroelectrics **315**, 123 (2005)

125. K. Sakata, Y. Masuda, Ferroelectrics **7**, 347 (1974)

126. J. Suchanicz, J. Kwapulinski, Ferroelectrics **165**, 249 (1995)

127. P.A. Thomas, S. Trujillo, M. Boudard, S. Gorfman, J. Kreisel, Solid State Sci. **12**, 311 (2010)

128. S.B. Vakhrushev, V.A. Isupov, B.E. Kvyatkovsky, N.M. Okuneva, I.P. Pronin, G.A. Smolensky, P.P. Syrnikov, Ferroelectrics **63**, 153 (1985)

129. M.-S. Zhang, J.F. Scott, J.A. Zvirgzds, Ferroelectr. Lett. **6**, 147 (1986)

130. E. Sapper, S. Schaab, W. Jo, T. Granzow, J. Rödel, J. Appl. Phys. **111**, 014105 (2012)

131. M.B. Rauls, W. Dong, J.E. Huber, C.S. Lynch, Acta Mater. **59**, 2713 (2011)

132. T. Tsurumi, K. Soejima, T. Kamiya, M. Daimon, Jpn. J. Appl. Phys. **33**, 1959 (1994)

133. G.A. Smolenskii, Jpn. J. Phys. Soc. **S28**, 26 (1970)

134. G.A. Smolenskii, V.A. Isupov, A.I. Agranovskaya, S.N. Popov, Sov. Phys. Solid State **2**, 2584 (1961)

135. D. Viehland, S.J. Jang, L.E. Cross, M. Wuttig, J. Appl. Phys. **68**, 2916 (1990)

136. C.A. Randall, A.S. Bhalla, T.R. Shrout, L.E. Cross, J. Mater. Res. **5**, 829 (1990)

137. V. Westphal, W. Kleemann, M. Glinchuk, Phys. Rev. Lett. **68**, 847 (1992)

138. A.E. Glazounov, A.K. Tagantsev, A.J. Bell, Phys. Rev. B **53**, 11281 (1996)

139. M.A. Akbas, P.K. Davies, J. Am. Ceram. Soc. **80**, 2933 (1997)

140. R. Pirc, R. Blinc, Phys. Rev. B **60**, 13470 (1999)

141. W. Kleemann, J. Mater. Sci. **41**, 129 (2006)

142. V. Bobnar, Z. Kutnjak, R. Pirc, A. Levstik, Phys. Rev. B: Condens. Matter **60**, 6420 (1999)

143. R. Farhi, M.E. Marssi, J.L. Dellis, J.C. Picot, A. Morell, Ferroelectrics **176**, 99 (1996)

144. D. Viehland, M. Wuttig, L.E. Cross, Ferroelectrics **120**, 71 (1991)

145. D. Lin, K.W. Kwok, H.W.L. Chan, J. Phys. D: Appl. Phys. **40**, 5344 (2007)

146. X. Tan, E. Aulbach, W. Jo, T. Granzow, J. Kling, M. Marsilius, H.J. Kleebe, J. Rödel, J. Appl. Phys. **106**, 044107 (2009)

147. K. Wang, A. Hussain, W. Jo, J. Rödel, J. Am. Ceram. Soc. (2012) doi:10.1111/j.1551-2916.2012.05162.x

148. D. Schütz, M. Deluca, W. Krauss, A. Feteira, T. Jackson, K. Reichmann, Adv. Funct. Mater., online published (2012).

149. Y. Hiruma, Y. Imai, Y. Watanabe, H. Nagata, T. Takenaka, Appl. Phys. Lett. **92**, 262904 (2008)

150. Y. Hiruma, H. Nagata, T. Takenaka, J. Appl. Phys. **104**, 124106 (2008)

151. Y. Hiruma, H. Nagata, T. Takenaka, Jpn. J. Appl. Phys **48**, 09KC08 (2009)

152. Y. Hiruma, H. Nagata, T. Takenaka, Appl. Phys. Lett. **95**, 052903 (2009)

153. W. Krauss, D. Schütz, F.A. Mautner, A. Feteira, K. Reichmann, J. Eur. Ceram. Soc. **30**, 1827 (2010)

154. R. Zuo, C. Ye, X. Fang, J. Li, J. Eur. Ceram. Soc. **28**, 871 (2008)

155. W. Jo, E. Erdem, R.-A. Eichel, J. Glaum, T. Granzow, D. Damjanovic, J. Rödel, J. Appl. Phys. **108**, 014110 (2010)

156. W. Jo, J.-B. Ollagnier, J.-L. Park, E.-M. Anton, O.-J. Kwon, C. Park, H.-H. Seo, J.-S. Lee, E. Erdem, R.-A. Eichel, J. Rödel, J. Eur. Ceram. Soc. **31**, 2107 (2011)

157. A. Hussain, C.W. Ahn, J.S. Lee, A. Ullah, I.W. Kim, Sensors and Actuators A: Physical **158**, 84 (2010)

158. A. Hussain, C.W. Ahn, A. Ullah, J.S. Lee, I.W. Kim, Jpn. J. Appl. Phys. **49**, 041504 (2010)

159. V.-Q. Nguyen, H.-S. Han, K.-J. Kim, D.-D. Dang, K.-K. Ahn, J.-S. Lee, J. Alloy. Compd. **511**, 237 (2012)

160. K.-N. Pham, A. Hussain, C.W. Ahn, W. Kim, S.J. Jeong, J.-S. Lee, Mater. Lett. **64**, 2219 (2010)

161. K.T.P. Seifert, W. Jo, J. Rödel, J. Am. Ceram. Soc. **93**, 1392 (2010)

162. A. Ullah, C.W. Ahn, A. Hussain, S.Y. Lee, H.J. Lee, I.W. Kim, Curr. Appl. Phys. **10**, 1174 (2010)

163. E.-M. Anton, W. Jo, J. Trodahl, D. Damjanovic, J. Rödel, Jpn. J. Appl. Phys. **50**, 055802 (2011)

164. C.F. Pulvari, W. Kuebler, J. Appl. Phys. **29**, 1315 (1958)

165. N.A. Schmidt, Ferroelectrics **31**, 105 (1981)

166. M.H. Lente, Ferroelectrics **257**, 227 (2001)

167. R. Dittmer, W. Jo, E. Aulbach, T. Granzow, J. Rödel, J. Appl. Phys., accepted.

168. D. Lupascu, J. Rödel, Adv. Eng. Mater. **7**, 882 (2005)

169. M. Ehmke, J. Glaum, W. Jo, T. Granzow, J. Rödel, J. Am. Ceram. Soc. **94**, 2473 (2011)

170. Z. Luo, J. Glaum, T. Granzow, W. Jo, R. Dittmer, M. Hoffman, J. Rödel, J. Am. Ceram. Soc. **94**, 529 (2011)

171. Z. Luo, T. Granzow, J. Glaum, W. Jo, J. Rödel, M. Hoffman, J. Am. Ceram. Soc. **94**, 3927 (2011)

172. E.A. Patterson, D.P. Cann, IEEE Trans. Ultrason. Ferroelectr. Freq. Control **58**, 1835 (2011)

173. C.A. Randall, A. Kelnberger, G.Y. Yang, R.E. Eitel, T.R. Shrout, J. Electroceram. **14**, 177 (2005)

174. J. Juuti, M. Leinonen, H. Jantunen, in *Piezoelectric and acoustic materials for transducer applications*, ed. by A. Safari, E.K. Akdoğan (Springer, New York, 2008)

175. J. Koch, in *Dr. Alfred Hüthig Verlag GmbH* (Heidelberg, 1988)

176. K.G. Webber, E. Aulbach, J. Rödel, J. Phys. D: Appl. Phys. **43**, 365401 (2010)

177. R. Dittmer, E. Aulbach, W. Jo, K. G. Webber, J. Rödel, Scripta Mater. **67**(1), 100–03 (2012)

178. J. Zheng, S. Takahashi, S. Yoshikawa, K. Uchino, J. Am. Ceram. Soc. **79**, 3193 (1996)

179. M.S. Senousy, R.K.N.D. Rajapakse, D. Mumford, M.S. Gadala, Smart Mater. Struct. **18**, 045008 (2009)

180. H. Kanai, Y. Yamashita, O. Furukawa, M. Harata, Jpn. J. Appl. Phys., Part 1 **28**, 33 (1989)

181. A. Yoneda, T. Takenaka, K. Sakata, Jpn. J. Appl. Phys., Part 1 **28**, 95 (1989)

182. D.E. Dausch, F. Wang, G.H. Haertling, *ISAF '94 PROCEEDINGS of the Ninth IEEE International Symposium on Applications of Ferroelectrics, Pennsylvania State University, 701* (IEEE, New York, 1994)

183. O. Furukawa, M. Harata, M. Imai, Y. Yamashita, S. Mukaeda, J. Mater. Sci. **26**, 5838 (1991)

184. T.R. Shrout, W.A. Schulze, J.V. Biggers, Ferroelectrics **29**, 129 (1980)

185. T.R. Shrout, W.A. Schulze, J.V. Biggers, Ferroelectrics **34**, 105 (1981)

186. S. Tashiro, Y. Mizukami, H. Igarashi, Jpn. J. Appl. Phys., Part 1 **30**, 2311 (1991)

187. H. Komiya, Y. Naito, T. Takenaka, K. Sakata, Jpn. J. Appl. Phys., Part 1 **28**, 114 (1989)

188. D.E. Dausch, E. Furman, F. Wang, G.H. Haertling, Ferroelectrics **177**, 237 (1996)

189. D.S. Lee, D.H. Lim, M.S. Kim, K.H. Kim, S.J. Jeong, Appl. Phys. Lett. **99**, 062906 (2011)

190. G.H. Haertling, J. Am. Ceram. Soc. **82**, 797 (1999)

191. J. Chen, R. Panda, Ultrasonics Symposium, 2005 IEEE, 235 (2005)

192. X. Li, H. Luo, J. Am. Ceram. Soc. **93**, 2915 (2010)

193. S. Zhang, F. Li, J. Appl. Phys. **111**, 031301 (2012)

194. S.-E. Park, T.R. Shrout, J. Appl. Phys. **82**, 1804 (1997)

195. S. Wada, K. Yako, K. Yokoo, H. Kakemoto, T. Tsurumi, Ferroelectrics **334**, 17 (2006)

196. S.A. Sheets, A.N. Soukhojak, N. Ohashi, Y.-M. Chiang, J. Appl. Phys. **90**, 5287 (2001)

197. K. Chen, G. Xu, D. Yang, X. Wang, J. Li, J. Appl. Phys. **101**, 044103 (2007)

198. J.G. Fisher, A. Benčan, J. Bernard, J. Holc, M. Kosec, S. Vernay, D. Rytz, J. Eur. Ceram. Soc. **27**, 4103 (2007)

199. Y. Inagaki, K.-I. Kakimoto, Appl. Phys. Express **1**, 061602 (2008)

200. Y. Kizaki, Y. Noguchi, M. Miyayama, Appl. Phys. Lett. **89**, 142910 (2006)

201. D. Lin, Z. Li, S. Zhang, Z. Xu, X. Yao, Solid State Commun. **149**, 1646 (2009)

202. J. Bubesh Babu, G. Madeswaran, M. He, D.F. Zhang, X.L. Chen, R. Dhanasekaran, J. Cryst. Growth **310**, 467 (2008)

203. W. Ge, H. Liu, X. Zhao, X. Pan, T. He, D. Lin, H. Xu, H. Luo, J. Alloys Compd. **456**, 503 (2008)

204. W. Ge, H. Liu, X. Zhao, W. Zhong, X. Pan, T. He, D. Lin, H. Xu, X. Jiang, H. Luo, J. Alloys Compd. **462**, 256 (2008)

205. Y. Hosono, K. Harada, Y. Yamashita, Jpn. J. Appl. Phys., Part 1 **40**, 5722 (2001)

206. K.-S. Moon, D. Rout, H.-Y. Lee, S.-J.L. Kang, J. Cryst. Growth **317**, 28 (2011)

207. S. Teranishi, M. Suzuki, N. Noguchi, M. Miyayama, C. Moriyoshi, Y. Kuroiwa, K. Tawa, S. Mori, Appl. Phys. Lett. **92, 182905 (2008)**

208. S. Trujillo, J. Kreisel, Q. Jiang, J.H. Smith, P.A. Thomas, P. Bouvier, F. Weiss, J. Phys. Condens. Matter **17**, 6587 (2005)

209. C.S. Tu, S.H. Huang, C.S. Ku, H.Y. Lee, R.R. Chien, V.H. Schmidt, H. Luo, Appl. Phys. Lett. **96**, 062903 (2010)

210. G. Xu, Z. Duan, X. Wang, D. Yang, J. Cryst. Growth **275**, 113 (2005)

211. K. Yamamoto, M. Suzuki, Y. Noguchi, M. Miyayama, Jpn. J. Appl. Phys., Part 1 **47**, 7623 (2008)

212. X. Yi, H. Chen, W. Cao, M. Zhao, D. Yang, G. Ma, C. Yang, J. Han, J. Cryst. Growth **281**, 364 (2005)

213. Q. Zhang, Y. Zhang, F. Wang, Y. Wang, D. Lin, X. Zhao, H. Luo, W. Ge, D. Viehland, Appl. Phys. Lett. **95**, 102904 (2009)

214. J.E. Daniels, W. Jo, J. Rödel, D. Rytz, W. Donner, Appl. Phys. Lett. **98**, 252904 (2011)

215. D. Fu, M. Endo, H. Taniguchi, T. Taniyama, S.-Y. Koshihara, M. Itoh, Appl. Phys. Lett. **92**, 172905 (2008)

216. Z. Yu, R. Guo, A.S. Bhalla, Mater. Lett. **57**, 349 (2002)

217. K. Uchida, T. Kikuchi, J. Am. Ceram. Soc. **61**, 5 (1978)

218. M. Spreitzer, M. Valant, D. Suvorov, J. Mater. Chem. **17**, 185 (2007)

219. A. Li, J. Wu, S. Qiao, W. Wu, B. Wu, D. Xiao, J. Zhu, physica status solidi (a), online published (2012).

220. Y.S. Sung, J.M. Kim, J.H. Cho, T.K. Song, M.H. Kim, H.H. Chong, T.G. Park, D. Do, S.S. Kim, Appl. Phys. Lett. **96**, 022901 (2010)

221. Y.S. Sung, J.M. Kim, J.H. Cho, T.K. Song, M.H. Kim, T.G. Park, Appl. Phys. Lett. **98**, 012902 (2011)

222. W. Jo, D.-Y. Kim, N.-M. Hwang, J. Am. Ceram. Soc. **89**, 2369 (2006)

223. "Piezoelectric Actuators and Motors - Global Markets and Market Trends," by Innovative Research and Products, Inc (Stamford, CT, USA, www.innoresearch.net)

224. W. Jo, J.E. Daniels, J.L. Jones, X. Tan, P.A. Thomas, D. Damjanovic, J. Rödel, J. Appl. Phys. **109**, 014110 (2011)

225. Y. Wang, A. B. Kounga Njiwa, C. Hoffmann, WO/2011/012682, 2011